

Mapping circumstellar magnetic fields of late-type evolved stars with the Goldreich-Kylafis effect: CARMA observations at $\lambda 1.3$ mm of R Crt and R Leo

KO-YUN HUANG,¹ ATHOL J. KEMBALL,¹ WOUTER H.T. VLEMMINGS,² SHIH-PING LAI,³ LOUIS YANG,⁴ AND IVÁN AGUDO⁵

¹*Department of Astronomy, University of Illinois at Urbana-Champaign, 1002 W. Green Street, Urbana, IL 61801 MC-221*

²*Department of Space, Earth and Environment, Chalmers University of Technology, Onsala Space Observatory, 439 92 Onsala, Sweden*

³*Institute of Astronomy and Department of Physics, National Tsing Hua University, Hsinchu 30013, Taiwan*

⁴*Kavli Institute for the Physics and Mathematics of the Universe (IPMU), University of Tokyo, Japan*

⁵*Instituto de Astrofísica de Andalucía (CSIC), Glorieta de la Astronomía s/n 18008 Granada, Spain*

(Accepted June 28, 2020)

Submitted to ApJ

Keywords: Asymptotic giant branch stars – stellar magnetic fields – polarimetry – CO line emission – circumstellar masers

ABSTRACT

Mapping magnetic fields is the key to resolving what remains an unclear physical picture of circumstellar magnetic fields in late-type evolved stars. Observations of linearly polarized emission from thermal molecular line transitions due to the Goldreich-Kylafis (G-K) effect provides valuable insight into the magnetic field geometry in these sources that is complementary to other key studies. In this paper, we present the detection of spectral-line polarization from both the thermal $J = 2 - 1$ CO line and the $v = 1, J = 5 - 4$ SiO maser line toward two thermal-pulsating (TP-) AGB stars, R Crt and R Leo. The observed fractional linear polarization in the CO emission is measured as $m_l \sim 3.1\%$ and $m_l \sim 9.7\%$ for R Crt and R Leo respectively. A circumstellar envelope (CSE) model profile and the associated parameters are estimated and used as input to a more detailed modeling of the predicted linear polarization expected from the G-K effect. The observed thermal line polarization level is consistent with the predicted results from the G-K model for R Crt; additional effects need to be considered for R Leo.

1. INTRODUCTION

Key uncertainties remain concerning the morphology and magnitude of magnetic fields in the circumstellar environments (CSEs) around late-type evolved stars (Leal-Ferreira et al. 2013; Lèbre et al. 2014; Duthu et al. 2017). This includes the relative dynamical influence of magnetic fields in shaping mass-loss outflows from TP-AGB stars relative to competing mechanisms such as wind interaction models and binarity (García-Segura et al. 1999, 2014; Matt et al. 2000; Blackman et al. 2001; Soker 2006; Kwok et al. 1978; Frank et al. 1993; Balick & Frank 2002; Soker 2004; García-Segura et al. 2018; Frank et al. 2018).

The interstellar magnetic field may be traced by observations of dust continuum polarization (Lazarian 2007; Hoang & Lazarian 2008), the Zeeman effect (Crutcher 2012; Goldreich et al. 1973; Elitzur 1996), and the Goldreich-Kylafis (G-K) effect (Goldreich & Kylafis 1981, 1982; Kylafis 1983a; Deguchi & Watson 1984; Lis et al. 1988; Cortes et al. 2005). In the current work we present continuum and molecular line polarization observations at 1.3mm wavelength with the Combined Array for Research in Millimeter-wave Astronomy (CARMA¹) of the CSE toward the TP-AGB stars R Leo and R Crt. Our goal is to use the joint and complementary constraints provided by these three methods to explore the circumstellar magnetic field of late-type evolved stars and to illuminate CSE evolution between the post-AGB and proto-planetary nebulae (PNe) phases.

Dust polarization observations allow the magnetic field morphology to be inferred in the plane of the sky from aligned dust grain emission (Lazarian 2007) but do not provide the field magnitude (Crutcher 2012).

¹ <https://www.mmarray.org>

The Zeeman effect in both thermal and maser line emission is the primary technique for measuring magnetic field strength directly, particularly for paramagnetic species, as reviewed by [Crutcher & Kemball \(2019\)](#). Given the intrinsic compactness and brightness of maser components, in high angular resolution polarization observations they act as vital probes of the magnetic field at small spatial scales, including shock-enhanced and higher density regions in the CSE ([Reid & Moran 1981](#); [Gray 2012](#); [Moran et al. 1979](#); [Elitzur 1980](#); [Miyoshi et al. 1994](#); [Diamond et al. 1994](#)). Molecular species observed include SiO ([Kemball & Diamond 1997](#); [Diamond & Kemball 2003](#); [Kemball et al. 2009](#)), H₂O ([Fiebig & Guesten 1989](#); [Vlemmings et al. 2006](#)), and OH ([Kemball & Diamond 1993](#)). Such observations, coupled with a radiative transport model for polarized maser emission, allow the inference of both the projected magnetic field direction and magnitude in principle. In practice there are ambiguities due to uncertainties in polarized maser radiation transport theory ([Watson 2009](#); [Gray 2012](#)).

The G-K effect produces linear polarization in thermal line emission induced by anisotropic velocity gradients that produce an anisotropic radiation field or an intrinsic radiation anisotropy in the presence of a magnetic field $\gtrsim 1\mu\text{G}$ ([Goldreich & Kylafis 1981](#); [Kylafis 1983a](#)). Under the large velocity gradient approximation (LVG) ([Sobolev 1960](#)) a velocity gradient produces a gradient in optical depth. This yields a net linear polarization in the line emission either parallel or perpendicular to the local magnetic field. This ambiguity can be resolved through careful modeling ([Goldreich & Kylafis 1981](#); [Cortes et al. 2005](#); [Yang & Lai 2010](#)). G-K observational studies have been undertaken toward molecular clouds ([Lai et al. 2003](#); [Cortes et al. 2005](#); [Li & Henning 2011](#)), star-forming region outflows and jets ([Ching et al. 2016](#); [Lee et al. 2018](#)), AGB stars ([Wannier et al. 1983](#); [Glenn et al. 1997](#); [Vlemmings et al. 2012](#); [Girart et al. 2012](#)), red supergiant (RSG) stars ([Vlemmings et al. 2017](#)), and PNe ([Sabin et al. 2014](#)). The principal advantage of G-K effect observations is probe field morphology in depth; the CSE contains a range of molecular species with varying chemical stratification and excitation profiles over the envelope. The G-K polarization signal also arises from underlying physics that is distinct from the generating mechanisms for continuum dust polarization and the Zeeman effect. It is therefore subject to different observational and theoretical systematic errors.

The measured radial power-law index of the ABG CSE magnetic field strength ([Reid et al. 1979](#); [Reid 1990](#); [Leal-Ferreira et al. 2013](#)) has been estimated from the Zeeman effect in various molecular species ([Herpin et al. 2006](#); [Leal-Ferreira et al. 2013](#); [Duthu et al. 2017](#), and references therein). There are competing arguments concerning the magnitude, origin, morphology, and dynamical influence AGB circumstellar magnetic fields ([Blackman et al. 2001](#); [Thomas et al. 1995](#); [Nordhaus & Blackman 2006](#); [Soker 2006](#); [Soker & Zoabi 2002](#); [Soker 2002](#)). [Lèbre et al. \(2014\)](#) report optical spectropolarimetric observations of the S-type Mira star χ Cyg that infer a surface-averaged magnetic field strength of ~ 0.5 G. These authors argue against a global dipole or poloidal morphology due to the implied photospheric field strengths ($B \sim 10^{2-3}$ G). In conjunction with optical spectropolarimetry of the non-rotating RSG Betelgeuse ([Petit et al. 2013](#)), they argue for local fields arising from convective dynamos ([Soker 2006](#); [Dorch 2004](#)).

Localized magnetic field enhancement has been proposed above stellar magnetic spots ([Soker 2002](#)) or as a result of pulsation shock compression of the tangential field ([Hartquist & Dyson 1997](#); [Kemball et al. 2009](#); [Richter et al. 2016](#)). Maser polarization magnetic field strengths imply a magnetic energy density exceeding the thermal and ram pressure ([Reid 2007](#); [Richter et al. 2016](#)). Further, [Watson \(2009\)](#) argues that the measured circular SiO maser polarization may arise from non-Zeeman effects. Both factors have been used to argue against the hypothesis of a global dynamically-significant magnetic field. However, recent G-K observations of CO emission toward OH17.7-2.0 ([Vlemmings 2019](#)) suggest a global field morphology consistent with prior OH maser observations. The morphology, magnitude, and dynamical influence of magnetic fields in late-type evolved stars therefore remains a critical open question in both theory and observation ([Vlemmings 2019](#)).

The role magnetic fields play in developing axisymmetry from TP-AGB to PNe evolutionary phases is presently unclear ([Blackman et al. 2001](#); [Nordhaus & Blackman 2006](#); [García-Segura et al. 1999, 2014](#)). Outflow collimation ([van Marle et al. 2014](#)) and direct shaping of the CSE material around isolated AGB stars ([Rüdiger et al. 2005](#); [Nordhaus et al. 2007](#)) have both been attributed to magnetic fields. High angular resolution studies of total intensity and magnetic field morphology in AGB stars are needed to further inform this issue.

Target source properties follow and are summarized in Table 1, including the right ascension and declination (J2000), chemical classification, variability type, pulsation period P (days), and distance (pc) for each star.

The results presented here are believed to be the only spectral-line CARMA polarimetry of late-type evolved stars at $\lambda = 1.3\text{mm}$. We detect linear polarization in the CO thermal emission at the level $m_l \sim 3 - 9\%$ which we believe is due to the G-K effect. Associated modeling and analysis are presented.

The paper is structured as follows. In Section 2, we describe the observations and data reduction process. The observational results are presented in Section 3. Subsequent modeling, analysis, and discussion are outlined in Section 4 and conclusions are presented in Section 5.

1.1. *R Crt*

R Crt is a semiregular (SRb) AGB star at a parallax distance 236 pc (Gaia Collaboration et al. 2018; Luri et al. 2018) with a pulsation period of 160 days (Samus’ et al. 2017) and a mass-loss rate $\dot{M} \sim 8 \times 10^{-7} [M_{\odot}/\text{yr}]$ (Paladini et al. 2017). It has been found that the Gaia parallax results for the extended, pulsating, and bright AGB stars are often unreliable (van Langevelde et al. 2018; Xu et al. 2019; Ramstedt et al. 2020). As discussed in Ramstedt et al. (2020) this is even true for stars with what appear to be good astrometric solutions, such as R Crt. However, since R Crt is an SRb variable star, this could also imply significant uncertainties when using a Period-Luminosity (P-L) distance (Feast et al. 1989); accordingly we adopt the Gaia distance for R Crt. Adopted distances in Section 1.1 and 1.2 are used only in establishing Figure length scales in this paper. The inferred magnetic field strength from single-dish SiO maser Zeeman observations ranges from $B \sim 0.0 - 3.7$ G over spectral components (Herpin et al. 2006). R Crt has been identified with a companion star (Proust et al. 1981; Cox et al. 2012), and is believed to harbor an outflow structure (Ishitsuka et al. 2001; Kim et al. 2018) possibly aligned with the magnetic field direction inferred from OH maser observations (Szymczak et al. 1999).

1.2. *R Leo*

R Leo is a nearby, typical M-type AGB star with a P-L distance of 95 pc (Matthews et al. 2018) derived using Feast et al. (1989) and data from Haniff et al. (1995). It has been intensively studied in several molecular lines including: SiO lines (e.g. Cotton et al. 2009; de Vicente et al. 2016; Herpin et al. 2006), H₂O masers (e.g. Menten & Melnick 1991; Yates et al. 1995), OH masers (e.g. Fish et al. 2006; Etoka & Le Squeren 1997), CO thermal lines (e.g. Ramstedt & Olofsson 2014; De Beck et al. 2010; Teyssier et al. 2006), and HCN thermal lines (Schöier et al. 2013). The dust shell properties have been observed in infrared and radio continuum (e.g. Wittkowski et al. 2016; Ireland et al. 2004; Schöier et al. 2013); R Leo shows statistically-significant deviations from sphericity in its radio photosphere (Matthews et al. 2018; Reid & Menten 2007) and its dusty environment (Paladini et al. 2017). The pulsation period of R Leo is 310 days (Whitelock & Feast 2000; Samus’ et al. 2017) and the mass-loss rate estimate is $\dot{M} \sim 1.1 \times 10^{-7} [M_{\odot}/\text{yr}]$ (Danilovich et al. 2015). The magnetic field strength in the near CSE of R Leo is estimated from single-dish SiO maser Zeeman observations to be: $B \sim 4.2 - 4.6$ G (Herpin et al. 2006). R Leo has also been suggested as hosting a Jovian planet remnant (Wiesemeyer et al. 2009). Recent ALMA observations of R Leo (Vlemmings et al. 2019) provide important insight into the extended atmosphere region $R \sim 1 - 2R_{*}$ and measure an asymmetric expansion with a mean velocity of 10.6 ± 1.4 km/s.

Table 1. Source information

Name	RA (J2000)	Dec (J2000)	Chem. class	Variability	P (days)	Distance (pc)
R Crt	11:00:33.85	-18:19:29.85	O-rich ^(a)	SRb ^(a)	160 ^(a)	236 ^(b)
R Leo	09:47:33.49	+11:25:43.67	O-rich ^(a)	Mira ^(a)	309.95 ^(a)	95 ^(c)

- a. Chemical classification, variability type, and pulsation period P are from Samus’ et al. (2017).
b. Parallax distance estimate is from Gaia DR2 (Gaia Collaboration et al. 2018; Luri et al. 2018).
c. P-L distance estimate is from Matthews et al. (2018).

2. OBSERVATION AND DATA REDUCTION

2.1. Observation

The observations of R Crt and R Leo were performed in the CARMA E-configuration (8.5 – 66 m baseline lengths). Two observing runs were performed, on November 16, 2014 and November 11, 2014 respectively, with each run of total duration 3.7 hours. The correlator was configured in full Stokes mode to observe the SiO $v = 1, J = 5 - 4$ line in the lower sideband (LSB) and the CO $J = 2 - 1$ line in the upper sideband (USB), with adopted transition rest frequencies of 215.596 GHz and 230.538 GHz respectively (Lovas et al. 2009). Both lines were observed in narrow-band

(line) spectral windows of bandwidth $\Delta\nu = 62.2$ MHz each sampled over 191 frequency channels with corresponding nominal velocity resolutions of 0.453 km/s and 0.423 km/s respectively. In addition, two wide-band (continuum) spectral windows each of bandwidth $\Delta\nu = 489.6$ MHz and sampled over 47 frequency channels each were centered on the spectral lines.

2.2. Data reduction

We describe the data reduction using the general interferometric data model developed by Hamaker et al. (1996) and Sault et al. (1996) adopting a circularly-polarized basis as used by CARMA. Here, 2×2 Jones calibration matrices $\mathbf{J}_m \in \{\mathbf{G}_m, \mathbf{B}_m, \mathbf{D}_m, \dots\}$ are used to represent all linear instrumental and propagation signal-path effects at each antenna m connecting the incident electric field $\mathbf{E}_m = [E_m^R, E_m^L]^T$ to the measured signal \mathbf{E}'_m . Jones matrix \mathbf{G}_m defines the net frequency-independent gain, \mathbf{B}_m the net frequency-dependent passband, and \mathbf{D}_m the instrumental polarization leakage. The radio-interferometric cross correlation on baseline m - n takes the form:

$$\begin{aligned} \mathbf{R}'_{mn} = \langle \mathbf{E}'_m \otimes \mathbf{E}'_n \rangle &= \left(\prod \mathbf{J}_m \otimes \mathbf{J}_n \right) \mathbf{R}_{mn} \\ &= [(\mathbf{G}_m \mathbf{B}_m \mathbf{D}_m \dots) \otimes (\mathbf{G}_n^* \mathbf{B}_n^* \mathbf{D}_n^* \dots)] \mathbf{R}_{mn} \end{aligned} \quad (1)$$

where \otimes denotes the outer matrix product and \mathbf{R}_{mn} is the intrinsic coherence. CARMA continuum polarimetry is described by Hull & Plambeck (2015). Polarization calibration for the pre-cursor Owens Valley Radio Observatory (OVRO) is described by Akeson (1997).

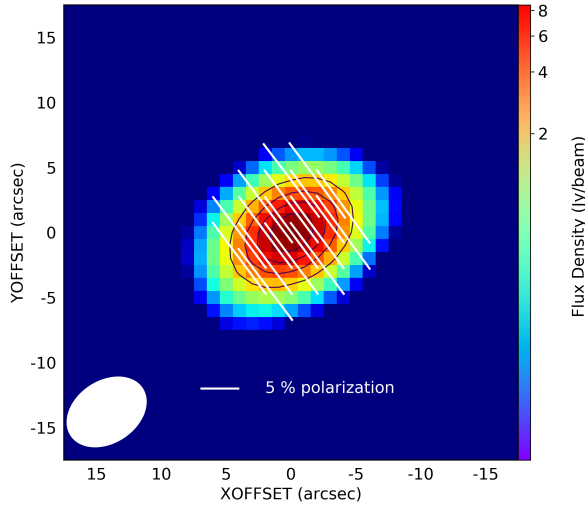
The parallel-hand (RR,LL) data calibration was performed using the CARMA Data REDuction pipeline, CADRE (Friedel 2013), based on the Multichannel Image Reconstruction, Image Analysis and Display analysis package (MIRIAD) (Sault et al. 1995). The parallel-hand reduction corrects the passband (\mathbf{B}_m) and gain (\mathbf{G}_m) calibration terms. The CADRE pipeline was extended to support full-polarization reduction. For R Crt, 3C279 was used as the bandpass, gain, and leakage calibrator. For R Leo, 3C84 was used as the bandpass calibrator, and OJ287 as the gain and leakage calibrator. The gain calibrator absolute flux densities were obtained from high-quality ALMA band 6 (211 – 275 GHz) calibrator catalogue² entries adjacent in time. The resulting flux densities were 8.38 ± 0.39 Jy (3C279) and 3.04 ± 0.17 Jy (OJ287). The antenna-based R and L gains $\mathbf{G}_m = \text{diag}(G_m^R, G_m^L) = \text{diag}(g_m^R e^{i\phi_m^R}, g_m^L e^{i\phi_m^L})$ were solved separately over time using the RR and LL data respectively. The underlying data were flagged for gain solutions showing high time-variability or outlier behavior in the differential polarization amplitude gain ratio $g_m^{R/L}$.

Full polarization calibration requires augmentation of parallel-hand reduction by: i) R-L phase ($\phi_{RL,m} = \phi_m^R - \phi_m^L$) calibration; and ii) polarization leakage (D-term, \mathbf{D}_m) calibration (Thompson et al. 2017; Hull & Plambeck 2015). At millimeter wavelengths $\phi_{RL,m}$ is primarily instrumental as the atmosphere is predominantly non-dispersive (Kemball & Richter 2011). The CARMA 10-m telescopes allow injected calibration of the R-L phase (Hull 2014; Hull & Plambeck 2015). The MIRIAD task `xyauto` solves for the R-L phase corrections for all the 10-m antennas using this method (Hull 2014; Hull & Plambeck 2015). The R-L solution from a reference 10-m antenna was then bootstrapped and applied to the 6-m antennas to correct their R-L phases using MIRIAD task `mfcal`. The instrumental polarization leakage term \mathbf{D}_m is solved for from the cross-polarized data (RL and LR) obtained on a bright calibrator source after parallel-hand calibration and correction for the residual R-L phase difference, for observations over a sufficient range $\Delta\alpha$ of parallactic angle coverage (Thompson et al. 2017). The \mathbf{D}_m terms were solved for using the MIRIAD task `gpca1` with `options = qusolve`.

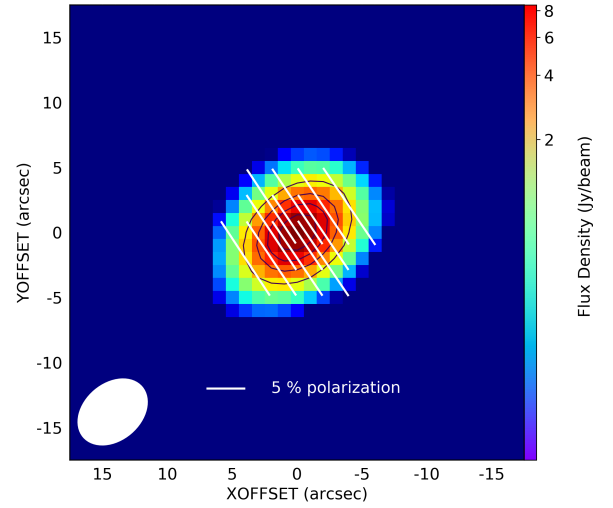
The IQUV images were formed from the fully calibrated visibilities by MIRIAD task `invert` using natural visibility gridding weighting. At 230 GHz, the beam size is $5.73'' \times 4.21''$ (at PA = 29.7°) for the calibrated R Crt data and $5.07'' \times 3.58''$ (at PA = 80.1°) for the calibrated R Leo data. The synthesized maps of linearly polarized intensity P were de-biased (Wardle & Kronberg 1974) using MIRIAD task `impol` and were masked below 5σ in Stokes I and 4σ in P . The spectral channels were averaged over 1 km s⁻¹ in both the CO and SiO channel maps. The final calibrated continuum maps of the gain calibrators, 3C279 and OJ287, are shown in Fig.1 and Fig.2. The calculated theoretical noise level in the spectral-line image cubes for a 1.0 km s⁻¹ channel width is between 29.6 mJy/beam (good weather) \sim 56.8 mJy/beam (typical weather)³. The measured median of the off-source noise over frequency from the spectral-line, total intensity data cubes is between 50.1 \sim 274.1 mJy/beam, over the separate transitions.

² <https://almascience.nrao.edu/alma-data/calibrator-catalogue>

³ <http://bima.astro.umd.edu/carma/observing/tools/rms.html>

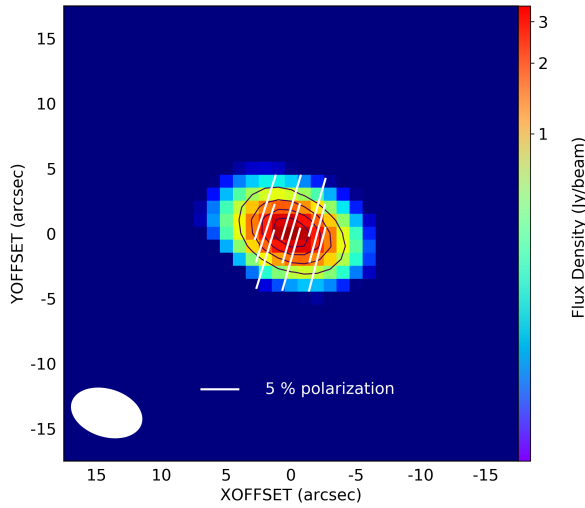


(a) Polarization map of 3C279, LSB

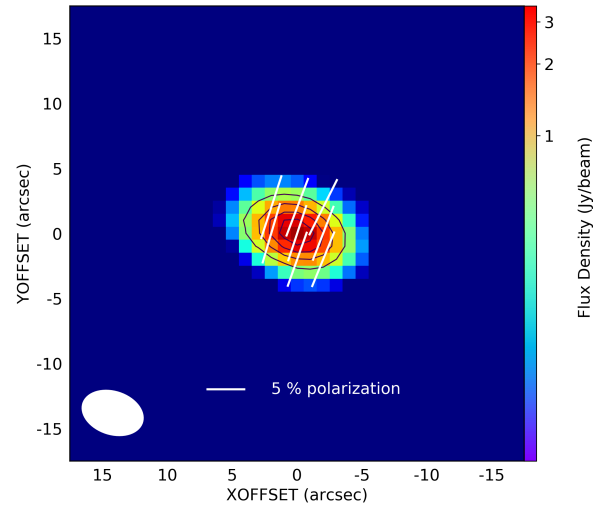


(b) Polarization map of 3C279, USB

Figure 1. Linear polarization maps of 3C279 in both LSB and USB. The color map shows the total intensity; the peak total intensity is 8.361 Jy/beam in LSB, and 8.363 Jy/beam in USB. The contour levels as the linear polarization intensity from 20%, 40%, 60%, and 80% of the maximum linear polarization intensity, which is 0.968 Jy/beam in LSB, and 0.967 Jy/beam in USB respectively. The synthesized beam is shown at lower left.



(a) Polarization map of OJ287, LSB



(b) Polarization map of OJ287, USB

Figure 2. Linear polarization maps of OJ287 in both LSB and USB. The color map shows the total intensity; the peak total intensity is 3.034 Jy/beam in LSB, and 3.029 Jy/beam in USB. The contour levels as the linear polarization intensity from 20%, 40%, 60%, and 80% of the maximum linear polarization intensity, which is 0.244 Jy/beam in LSB, and 0.230 Jy/beam in USB respectively. The synthesized beam is shown at lower left.

Several polarization and calibration quality assurance tests were applied to the fully calibrated data; these are described in Appendix A.

Table 2. Summary of the detected molecular lines of R Crt and R Leo in CARMA observation.

Source	Line	ν_0	F_ℓ	F_I
		[GHz]	[Jy beam ⁻¹ km s ⁻¹]	[Jy beam ⁻¹ km s ⁻¹]
R Crt	CO (J = 2-1)	230.538	3.60	433.9
	SiO (J=5-4, v=1)	215.596	1.31	27.9
R Leo	CO (J = 2-1)	230.538	2.62	297.9
	SiO (J=5-4, v=1)	215.596	89.9	492.3

Note: The listed are the rest frequency (ν_0) of the detected molecular lines, the integrated brightness over velocity channels of the linearly polarized intensity (F_ℓ) and total intensity (F_I) in each observation

3. RESULTS

In Table 2 the rest frequency ν_0 and the linearly-polarized intensity F_ℓ and total intensity F_I integrated over velocity are enumerated per source and molecular line. Total power spectra obtained by summing all total intensity points above 3σ in each image plane of the interferometric image cubes are shown in Fig. 3.

We detect continuum emission toward R Crt of 14.9 ± 2.4 mJy/beam in the LSB continuum spectral window and 18.3 ± 2.9 mJy/beam in the counterpart USB window. These values are measured at the peak-brightness pixel and the error is the off-source rms noise. In the same spectral windows, continuum emission is detected toward R Leo of 118.2 ± 3.2 mJy/beam in LSB and 123.0 ± 3.4 mJy/beam in USB using the same measurement methodology. No continuum polarization was detected toward either R Crt or R Leo, likely due to sensitivity limitations and the expected weakness of the dust continuum emission relative to the underlying stellar continuum. By comparison with the stellar continuum flux densities reported by [Vlemmings et al. \(2019\)](#) for R Leo, the dust contribution does not exceed $\sim 20\%$; a comparable result is expected for R Crt.

The $J = 2 - 1$ CO emission channel maps for both sources are displayed in Fig. 4. Contours depict linearly-polarized intensity P with associated vectors indicating EVPA χ ; both are overlaid on color plots of total intensity. Analogous channel maps for $v = 1, J = 5 - 4$ SiO emission are shown in Fig. 5. The peak-pixel linearly-polarized intensity P across these spectral-line image cubes is tabulated in Table 3 for each source and transition. We denote this as P_p . This table includes the associated LSR velocity v_{LSR} , point total intensity I_p and resulting fractional linear polarization $m_{l,p}$ at P_p . The error-weighted EVPA average $\bar{\chi}$ is computed over the angular (~ 10 arcsec) and frequency extent ($\Delta v \sim 2 - 4$ km/s) of the source for all pixel detections above 4σ . The statistical error σ_n in $\bar{\chi}$ was estimated by propagating the pixel error $\sigma_\chi = \sigma_P/2P$ ([Wardle & Kronberg 1974](#)) over the source summation ([Taylor 1996](#)). A conservative estimate of the systematic error (σ_s) in $\bar{\chi}$ was obtained from the absolute EVPA comparison against external measurements described in Appendix A. Based on the alignment uncertainty for 3C279, σ_s for R Crt is estimated as 10.8° ; similarly, via OJ287, σ_s for R Leo is estimated as 11.6° . The row σ in Table 3 is column-specific, namely σ_P for P_p , σ_I for I_p , and takes the format $\pm\sigma_n \pm \sigma_s$ for $\bar{\chi}$.

Table 4 lists the peak-pixel circularly-polarized intensity V_p in the $v = 1, J = 5 - 4$ SiO spectral-line image cube (Fig. 5) and associated LSR velocity v_{LSR} , point total intensity I_p and resulting degree of fractional circular polarization $m_{c,p}$ at V_p ; circular polarization is only detected toward R Leo.

4. ANALYSIS AND DISCUSSION

As shown in Table 3, the peak fractional linear polarizations for the $J = 2 - 1$ CO line emission are $m_l = 3.13\%$ and $m_l = 9.7\%$ for R Crt and R Leo respectively. In this section we describe numerical modeling to determine if this linear polarization can be ascribed to the G-K effect. Our modeling of the G-K effect in circumstellar CO requires as input radial CSE profiles in temperature $T(r)$ and density $n(r)$ in addition to a characterization of radiation anisotropy and velocity gradient structure; our adopted CSE model is described in Appendix B. In this section we also consider comparisons between the G-K signal, the SiO maser polarization, and further source properties in the literature.

4.1. G-K modeling

4.1.1. Framework

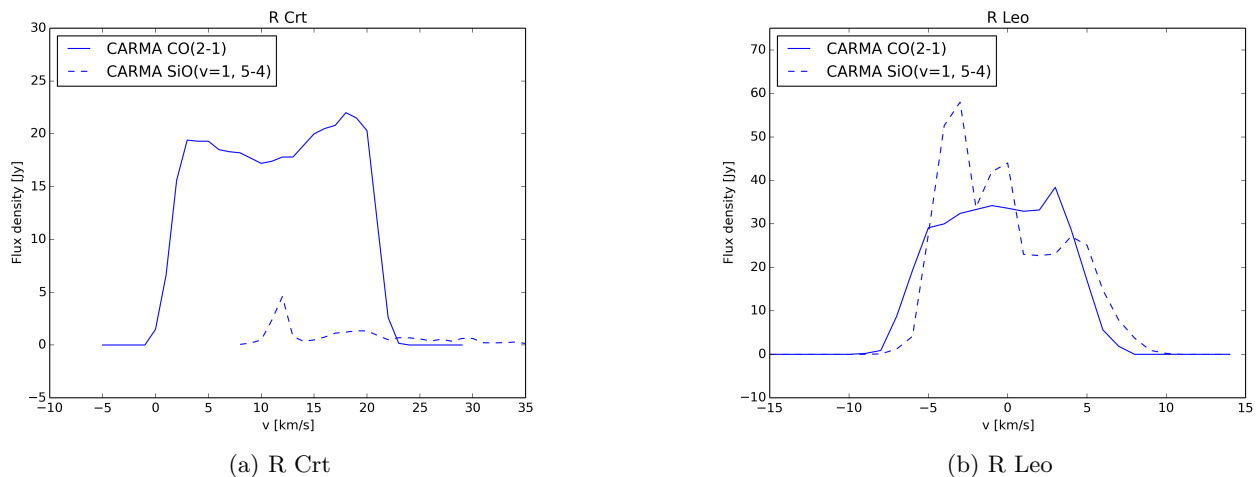
We use the G-K modeling framework developed independently by [Yang & Lai \(2010\)](#). The differences between the numerical code and prior approaches is described briefly here. Original work by [Goldreich & Kylafis \(1981, 1982\)](#) and

Table 3. Polarization properties at the position of peak linearly-polarized intensity in the spectral-line image cubes.

Source	Line	v_{LSR} [km s ⁻¹]	P_p [Jy beam ⁻¹]	I_p [Jy beam ⁻¹]	$m_{\ell,p}$ [%]	$\bar{\chi}$ [°]
R Crt	SiO (J=5-4, v=1)	12.0	0.778	4.52	17.2 (17.3 σ)	-15.4
	σ		0.045	0.05	-	$\pm 0.7 \pm 10.8$
	CO (J = 2-1)	20.0	0.361	11.44	3.13 (7.2 σ)	7.6
	σ		0.050	0.27	-	$\pm 1.0 \pm 10.8$
R Leo	SiO (J=5-4, v=1)	-4.0	18.67	53.98	34.6 (317 σ)	-1.1
	σ		0.06	0.17	-	$\pm 0.03 \pm 11.6$
	CO (J = 2-1)	4.0	0.375	3.86	9.71 (6.1 σ)	-77.7
	σ		0.062	0.14	-	$\pm 1.7 \pm 11.6$

Table 4. Polarization properties at the position of peak circularly-polarized intensity in the spectral-line image cubes.

Source	Line	v_{LSR} [km s ⁻¹]	V_p [Jy beam ⁻¹]	I_p [Jy beam ⁻¹]	$m_{c,p}$ [%]
R Crt	SiO (J=5-4, v=1)	-	-	-	-
	σ	-	-	-	-
R Leo	SiO (J=5-4, v=1)	-3.0	2.95	51.34	5.7 (40.3 σ)
	σ		0.07	0.17	-

**Figure 3.** Integrated spectra for both (a) R Crt, and (b) R Leo. The spectra were obtained by summing the total intensity at all points above 3σ in each image plane of the interferometric image cube using MIRIAD task `imspec`. The spectra are binned at a $\Delta v = 1$ km/s interval.

Kylafis (1983b) considered 1-D and 2-D LVG geometries, a $J = 1 - 0$ transition, and a collisional rate C to Einstein coefficient $A_{a,b}$ ratio of $\frac{C}{A_{a,b}} = 0.212$. Deguchi & Watson (1984) extended these calculations to multi-level transitions in CO, CS, and SiO using molecular data from Green & Chapman (1978) and Robinson & van Blerkom (1981). Cortes et al. (2005) moved further to include the influence of anisotropic radiation, a mixture of 1-D and 2-D LVG geometries, and updated molecular data from Flower (2001) motivated by their own observations and those of Lai et al. (2003). Yang & Lai (2010) developed an independent G-K numerical model incorporating these prior physical approaches, but excluding anisotropic radiation, and similarly focused on star formation. The code uses updated molecular data from the Leiden Atomic and Molecular Database (LAMDA) (Schöier et al. 2005). For technical details concerning the underlying algorithm implementation, we refer the reader to Yang & Lai (2010). In the current work the Yang & Lai (2010) G-K code was applied in a CSE environment and a source of radiative anisotropy was introduced to

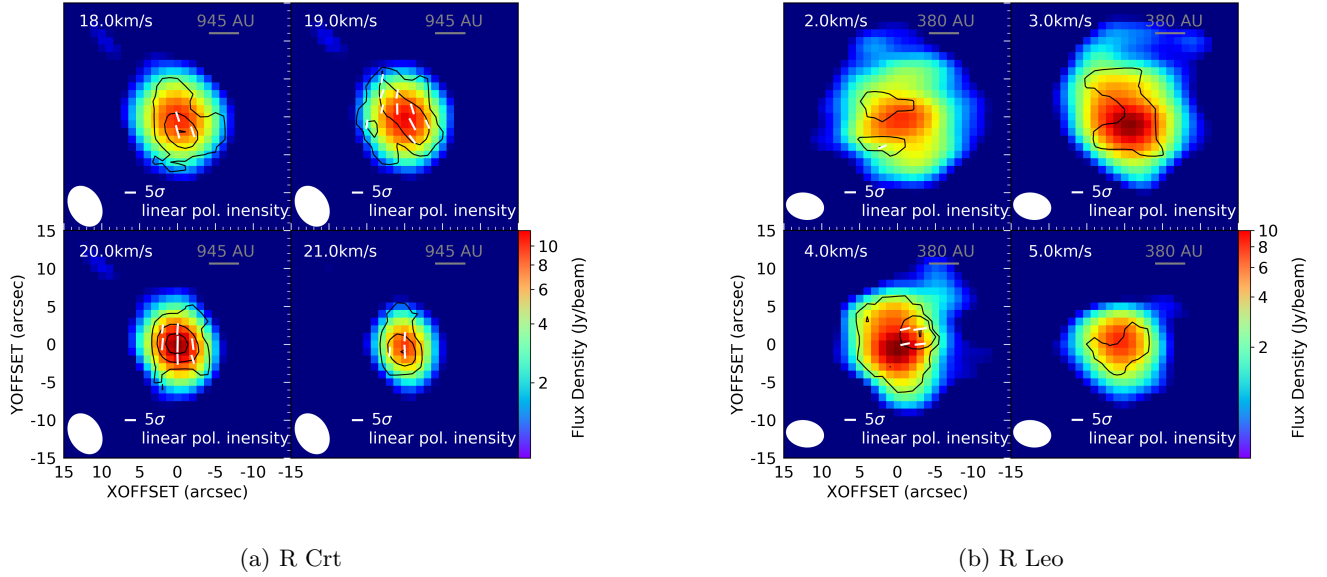


Figure 4. CO(2-1) spectral-line polarization maps of (a) R Crt, and (b) R Leo. The channels are averaged over interval of 1 km s^{-1} . The color map shows the spectral-line emission total intensity in log scale, and the contour levels of the linear polarization intensity are 2, 4, and 6 times σ where σ is the noise level of each source. The white segments are drawn at the EVPA orientation with scaled length proportional to linearly-polarized intensity. Beam size is also displayed at the lower-left corner in each map. The physical scale is derived from the adopted distances in Table 1.

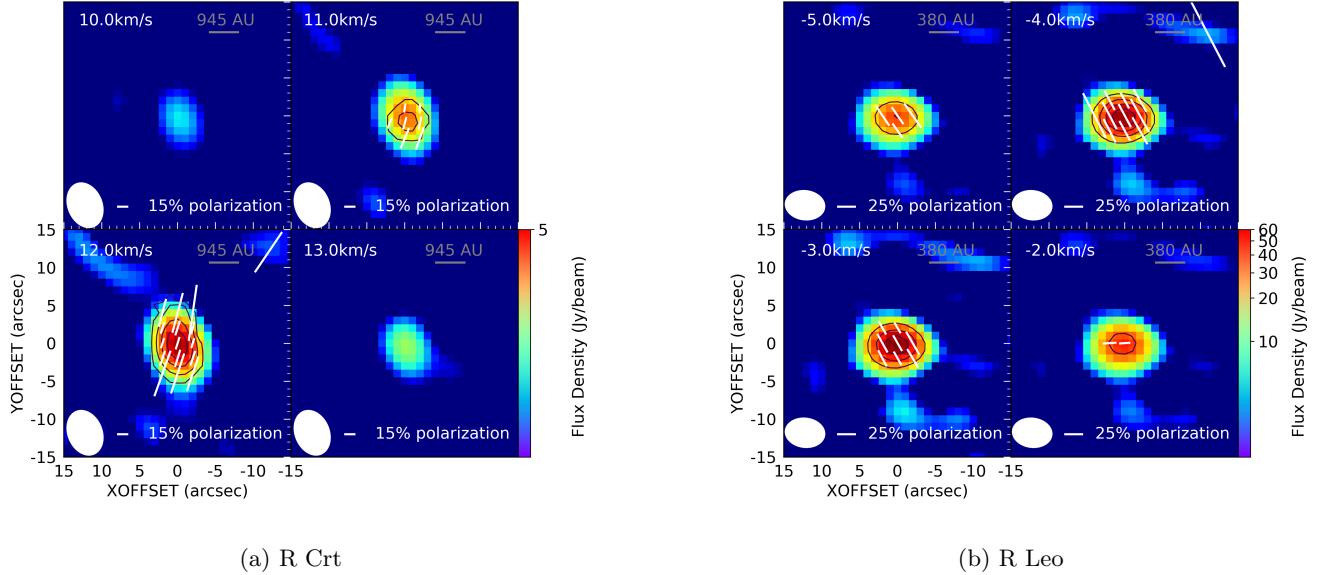


Figure 5. SiO(5-4, $v=1$) spectral-line polarization maps of (a) R Crt, and (b) R Leo. Again the channels are averaged over 1 km s^{-1} interval. The color corresponds to total intensity of the emission in log scale, contour levels as the linear polarization intensity from 20%, 40%, 60%, and 80% of the maximum, and white segments as the polarization angle with the scaled length as display of the linear polarization strength. The physical scale is derived from the adopted distances in Table 1.

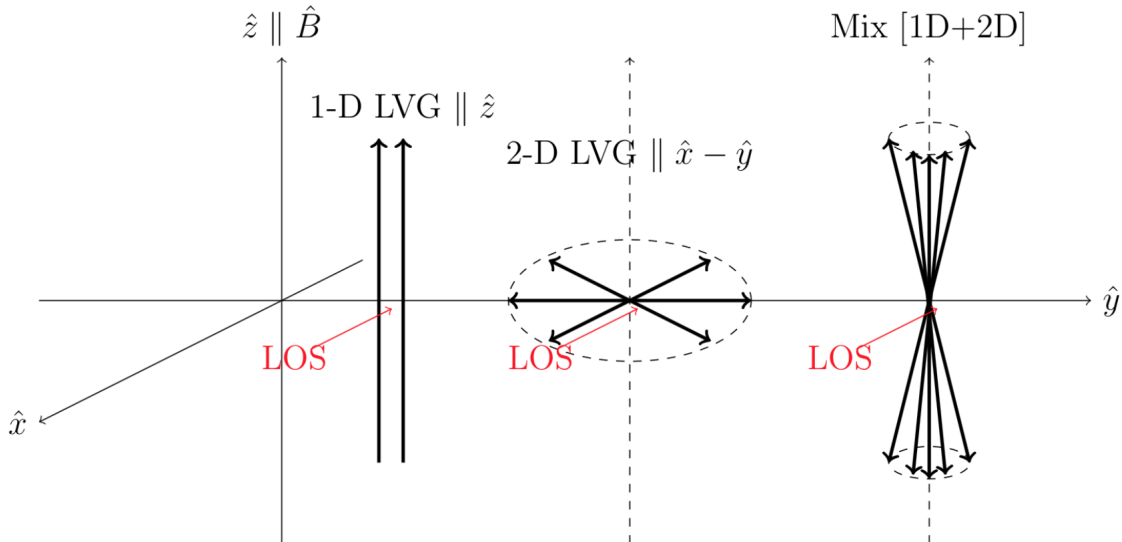


Figure 6. The schematic plot for three types of velocity gradient geometry as implemented in our existing G-K model (from left to right): i) 1-D velocity anisotropy parallel the magnetic field; ii) a 2-D velocity gradient along the 2-D plane perpendicular to the magnetic field; and, iii) a mixed model of (i) and (ii), yielding a cone-shaped velocity gradient lobe. The "LOS" label in red denotes the line-of-sight direction. The magnetic field orientation \hat{B} is set to be aligned with the z-axis, i.e. $\hat{z} \parallel \hat{B}$. And the black arrows in the plot point in the direction of the velocity gradient field. In our model we have adopted the mixed LVG velocity gradient geometry on the basis that of the three velocity gradient geometries, this model is closest to the modest axisymmetry that could reasonably be expected in the late AGB phase.

model emission from the central AGB star; this is discussed further in section 4.1.2. Representative densities and temperatures for the CSE, as tabulated in Table 6, differ from those in star-forming regions described above. The model used here considers an uniform magnetic field and uniform velocity gradient through the slab of material with constant thickness and density, as a first-order approximation. The code supports the following three types of velocity gradient geometry (as depicted in Fig. 6: i) 1-D velocity anisotropy parallel to the magnetic field; ii) a 2-D velocity gradient along the 2-D plane perpendicular to the magnetic field; and, iii) a mixed model of (i) and (ii), yielding a cone-shaped velocity gradient lobe. We used model (iii) to model bipolar outflows.

We note important new theoretical work by [Lankhaar & Vlemmings \(2020\)](#).

4.1.2. Observed linear polarization and the G-K model predictions

The predicted G-K fractional linear polarization is shown as a function of optical depth, temperature, and density in Fig. 7 for the CSE model described above and summarized in Table 6. A mixed LVG velocity gradient geometry (Fig. 8(iii)) was adopted in the G-K modeling as this geometry is closest to the modest axisymmetry possible in the late AGB phase. The effect of varying the velocity gradient geometry for a fixed representative temperature and density is shown in Fig. The legend in Fig. 7 indicates temperature (line color) and density (line style) thereby representing various effective distances from the central star. The densities are upper and lower bounds in Table 6 for $\beta \in \{0, 5\}$. For G-K emission, the sign $m_l < 0$ implies that the EVPA is parallel to the magnetic field. If the linear polarization in Fig. 4 is due to the G-K effect then the EVPA and magnetic field are aligned in the Figure 8.

Our G-K model predicts $m_l \sim 3\%$ (Fig. 7) which is consistent with our observational result for the CO emission toward R Crt. However, the fractional linear polarization $m_l \sim 9.7\%$ detected in CO toward R Leo exceeds our G-K modeling predictions. We note however that if the polarized emission originates from a region more compact than the associated Stokes I emission then interferometric spatial filtering (leading to missing flux density) may overestimate m_l .

An anisotropic radiation field can also contribute to linear polarization, reaching a maximum of order $m_l \sim 5 - 10\%$ ([Morris et al. 1985](#); [Cortes et al. 2005](#)). To explore this contribution we added an anisotropic radiation source in our G-K model. We considered the relative radio brightness of the central star and a dust clump at the dust-formation radius. The central star is assumed to be of order several thousand Kelvin and to subtend an angle ~ 0.01 rad from

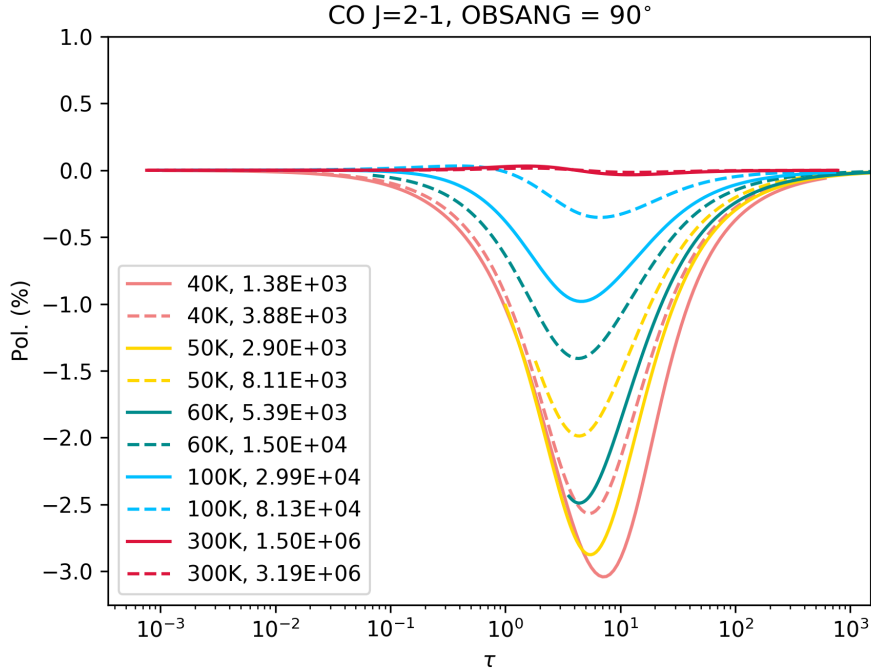


Figure 7. The predicted polarization signal level from our G-K modeling using mix model (corresponding to $\alpha = 0.1$ as discussed in Cortes et al. (2005)), density and temperature profile calculated based on R Leo case as listed in Table 6. The colors denote the temperature from low to high. The styles denote the lower bound (solid) and the upper bound (dashed) of the density profile listed in Table 6.

the circumstellar CO region at a radius $r \sim 200R_*$. Under these parameters the predicted G-K linear polarization peaks at the same optical depth as in Fig. 7 but m_l is not significantly increased. Over a broader parameter range of physical, and even unphysical, conditions we find that a fractional linear polarization exceeding $m_l > 5\%$ cannot readily be generated by our G-K model including anisotropic radiation.

We do not expect the fractional G-K linear polarization m_l to be identical between the sources due to differing local conditions (Fig. 4). (Vlemmings et al. 2012) report a value $m_l \sim 13\%$ for IK Tau in this CO transition although this value is similarly believed elevated due to interferometric flux density filtering in Stokes I .

Lastly, the uncertainty in T_* noted earlier translates to uncertainty in the CSE temperature following Equation B1 but does not have a significant effect on our inferred G-K linear polarization magnitude.

4.2. SiO maser polarization

We detect linear polarization in the $v = 1$, $J = 5 - 4$ SiO maser emission toward R Crt at $m_l \sim 17.2\%$ and R Leo at $m_l \sim 34.6\%$ (Table 3). At the closest matching velocities in the $v = 1$, $J = 2 - 1$ SiO maser spectra presented by Herpin et al. (2006) $m_l \sim 15\%$ for R Crt and $m_l \sim 26\%$ for R Leo. In the same $v = 1$, $J = 2 - 1$ SiO maser transition, Wiesemeyer et al. (2009) report a fractional linear polarization toward R Leo of $m_l \sim 24 - 26\%$. We note however that these are different SiO rotational transitions at differing spatial resolution and that SiO maser emission is highly time-variable (Pardo et al. 2004). Nonetheless these results are broadly consistent with the current work. Linear polarization in the current $v = 1$, $J = 5 - 4$ SiO maser transition has been observed toward other target sources including VY CMa at $m_l \sim 10 - 60\%$ (Shinnaga et al. 2004) and VX Sgr at $\langle m_l \rangle = 26 \pm 16\%$ (Vlemmings et al. 2011). Watson (2009) argues that high fractional linear polarization in circumstellar SiO maser emission (approaching $\sim 50\%$) would require an unphysical degree of maser saturation; higher values of m_l are more readily explained by anisotropic pumping. High fractional linear polarization in high- J SiO maser transitions strengthens the case for anisotropic pumping (Lankhaar & Vlemmings 2019).

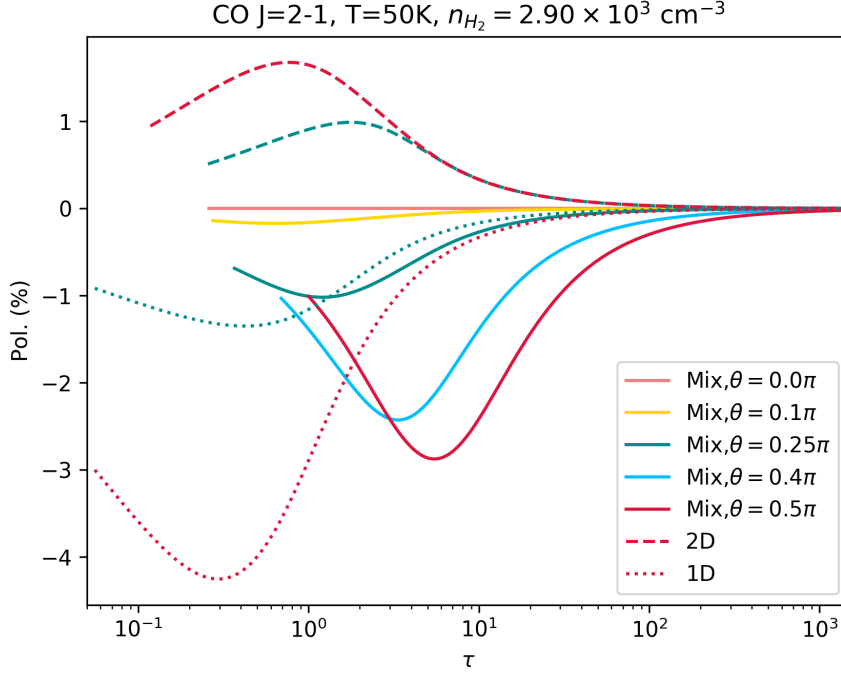


Figure 8. A comparison of the predicted G-K polarization profiles for the $J = 2 - 1$ CO line under various choices of velocity gradient geometries (Figure 6) and the line-of-sight (LOS) viewing angles. The angle θ (see color legend) refers to the angle between the LOS direction and the presumed magnetic field direction. Line style indicates the 1-D, 2-D, and Mix LVG geometry models. The CSE parameters used here are: $T = 50\text{K}$, $n(r) = 2.9 \times 10^3 \text{cm}^{-3}$.

We detect peak fractional circular polarization $m_c \sim 5.7\%$ in the $v = 1, J = 5 - 4$ SiO maser line toward R Leo (Table 3), but do not detect statistically significant circular polarization in this transition toward R Crt perhaps due to sensitivity. For reference, Herpin et al. (2006) report $m_c \sim 9 - 10\%$ toward R Leo in the $v = 1, J = 2 - 1$ SiO maser transition.

4.3. Comparison with other intrinsic alignments

In this section we consider the relation between the magnetic field orientation measured in the current work for R Crt and R Leo and other intrinsic alignments published for these sources in the literature. The compiled results are enumerated and described in Table 5. This table lists the intrinsic position angle (N through E), the observations (and telescope or instrument) from which this angle was inferred, and the corresponding citation. The compiled results are plotted schematically in Fig. 9 where the shaded opening angle indicates total uncertainty in orientation $\sigma_{tot} \sim \sqrt{\sigma_n^2 + \sigma_s^2}$, when available.

Several caveats apply when interpreting these alignment and orientation data. The measured SiO maser EVPA has a 90° ambiguity (\parallel, \perp) with respect to the magnetic field, depending on the angle between the line of sight and the magnetic field line relative to the Van Vleck angle $\theta_F \sim 55^\circ$ (Goldreich et al. 1973). SiO EVPA orientations are plotted accordingly with dashed lines in Fig. 9 to highlight this ambiguity. The physical conditions and associated radial distances sampled by the SiO, H_2O , OH, and CO molecules differ significantly as noted earlier. The length of each line is monotonically proportional to the distance scales traced by each transition, but not drawn strictly to scale for clarity of presentation. Fig. 9 shows that for R Crt, the measured angles are more narrowly confined compared to the case of R Leo.

5. CONCLUSIONS

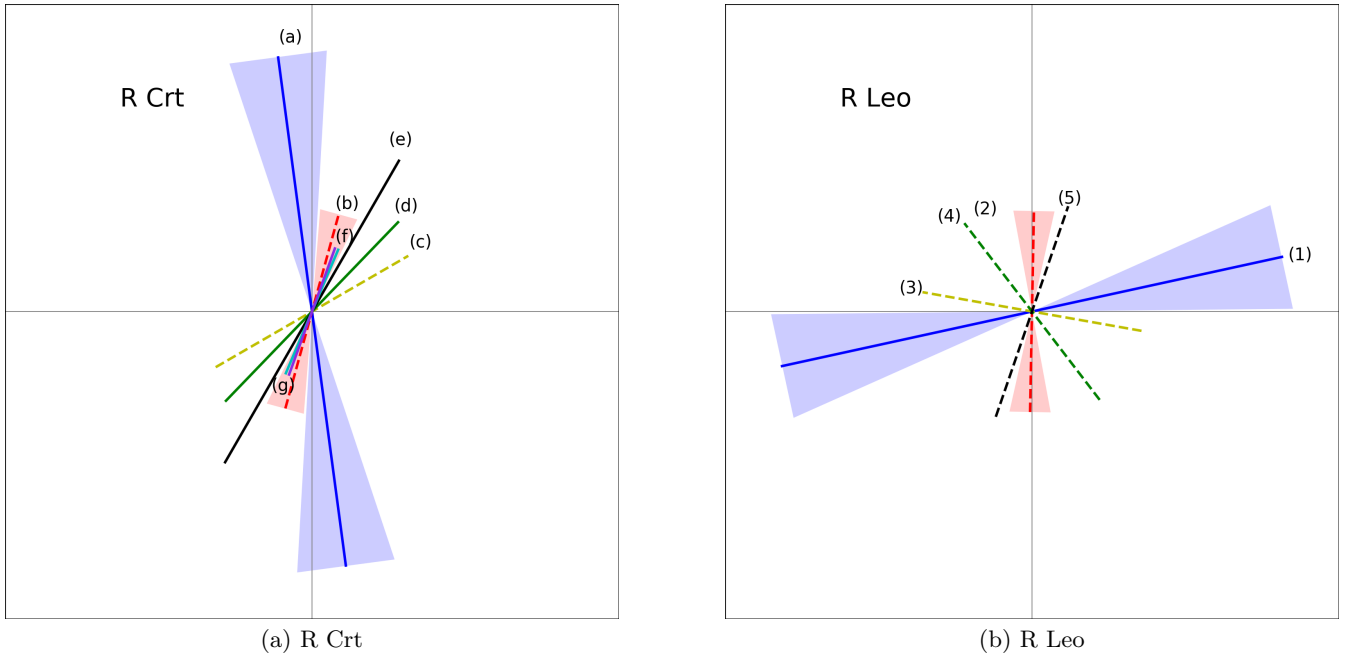
We have detected linear polarization in thermal $J = 2 - 1$ CO line emission from the CSE of the TP-AGB stars R Leo and R Crt in $\lambda 1.3$ mm full-Stokes observations with CARMA. The fractional linear polarization measured in the $J = 2 - 1$ CO line for R Crt ($m_l \sim 3.1\%$) is consistent with the predicted modeled G-K signal strength, while

Table 5. Intrinsic position angles and alignments measured for R Crt and R Leo.

Source	Position angle	Emission	Telescope or Instrument	Reference	Label
R Crt	$\phi_B = 7.6^\circ \pm 1.0^\circ \pm 10.8^\circ$	CO ($J = 2 - 1$)	CARMA	This work	(a)
	$\chi = -15.4^\circ \pm 0.7^\circ \pm 10.8^\circ$	SiO ($J = 5 - 4, v = 1$)	CARMA	This work	(b)
	$\chi = 120^\circ / -60^\circ$	SiO ($J = 2 - 1, v = 1$)	IRAM 30 m	(Herpin et al. 2006)	(c)
	$\phi_{outflow} = 136^\circ / -44^\circ$	H ₂ O maser	Japanese VLBI Network	(Ishitsuka et al. 2001)	(d)
	$\phi_B = -30^\circ$	OH 1667-MHz maser	MERLIN array	(Szymczak et al. 1999)	(e)
	$\phi_{star} = 157^\circ$	Mid-IR (Stellar elongation)	VLTI/MIDI	(Paladini et al. 2017)	(f)
	$\phi_{outflow} = 160^\circ$	Visible (Dust scattering)	VLT/SPHERE/ZIMPOL	(Khoury et al. 2020)	(g)
R Leo	$\phi_B = -77.7^\circ \pm 1.7^\circ \pm 11.6^\circ$	CO ($J = 2 - 1$)	CARMA	This work	(1)
	$\chi = -1.1^\circ \pm 0.03^\circ \pm 11.6^\circ$	SiO ($J = 5 - 4, v = 1$)	CARMA	This work	(2)
	$\chi = 80^\circ$	SiO ($J = 2 - 1, v = 1$)	IRAM 30 m	(Herpin et al. 2006)	(3)
	$\chi = [-40^\circ, -35^\circ]^a$	SiO ($J = 2 - 1, v = 1$)	IRAM 30 m	(Wiesemeyer et al. 2009)	(4)
	$\chi = -19^\circ \pm 65^\circ$	SiO ($J = 2 - 1, v = 1$)	NRAO 12 m Telescope	(Glenn et al. 2003)	(5)

^aThe listed EVPA range is extracted from their Fig.2; the geometric mean of this range is plotted in Figure 9.

NOTE—In this table, χ denotes an SiO emission EVPA, ϕ_B an inferred G-K magnetic field direction, $\phi_{outflow}$ an outflow direction, and ϕ_{star} the position angle of a stellar elongation.

**Figure 9.** Schematic plot from the compiled results. The labeling refers to the literature cited in Table 5

for R Leo the measured fractional linear polarization ($m_l \sim 9.7\%$) is higher than expected. Our G-K modeling is able to resolve the directional degeneracy, suggesting that the measured EVPA parallel to the magnetic field lines. We also have detected linear polarization in the $v = 1, J = 5 - 4$ SiO maser line toward the CSE of R Crt and R Leo in the range $m_l \sim 17 - 34\%$. We detect circular polarization in this maser line toward R Leo but not toward R Crt, the latter possibly due to sensitivity limitations. We detect continuum emission toward R Crt and R Leo in the wide-band spectral windows. However, no successful detection of polarized continuum emission is achieved likely due to sensitivity limitations and the relative weakness of dust emission to the stellar continuum. These results with CARMA from both observation and modeling demonstrate that the G-K effect is a viable means of extracting information concerning magnetic field morphology in the CSE around late-type evolved stars at various depths in the envelope. These observations are profoundly sensitivity-limited compared to modern telescopes such as ALMA

but are the first such observations with CARMA and confirm the scientific importance of observations of this nature (Vlemmings et al. 2012). At greater sensitivity, future in-depth morphological mapping of the circumstellar magnetic field around late-type stars is possible using a range of molecular species and the associated transitions.

APPENDIX

A. POLARIZATION AND CALIBRATION QUALITY ASSURANCE

This Appendix described the polarization quality assurance tests applied to the fully calibrated data.

The amplitude of the derived polarization leakage terms $|\mathbf{D}_m|$, across all spectral windows and both observing runs, ranged from few percent to a maximum of $\sim 20\%$, consistent with results from prior CARMA continuum polarimetry (Hull & Plambeck 2015). Although the \mathbf{D}_m are known to depend on time and frequency, a moderate level of instrumental stability is expected. We therefore examined the rank correlation of the antenna-based $|\mathbf{D}_m|$ against those obtained from a separately-reduced CARMA continuum polarimetry archival data set⁴ (Bower 2014). The Spearman rank-order correlation (Zwillinger & Kokoska 1999), Kendall’s tau (Knight 1966), and the Pearson correlation coefficient (Pearson 1895) were computed using SciPy⁵ for both the R Crt and R Leo data, across all spectral windows, and against the values of $|D_m^R|$ and $|D_m^L|$ derived from the archival data. The correlation coefficients fell within the range $r \in [0.1 \sim 0.6]$ with a maximum of 15 antennas in the current data. A median value $r \sim 0.4$ was obtained, indicating moderate correlation.

In addition, the cross-polarized visibility data showed significantly less scatter when plotted in the Re-Im plane before and after polarization calibration. Similarly the statistical distribution of the R-L phase difference $\phi_{RL,m}$ measured from the visibility data was narrower after full polarization calibration. Further, the dynamic range of the calibrator polarized intensity maps improved from ~ 30 to ~ 150 after polarization calibration.

Underlying phase calibration accuracy was assessed from the phase structure function of the calibrated parallel-hand visibility data in the continuum windows for the calibrators, averaged over frequency. For R Crt, the residual phase rms obtained is $\sigma_\phi \sim 9.8^\circ$ and for R Leo $\sigma_\phi \sim 17.0^\circ$. Both phase structure functions showed a slow increase of $\sim 10^\circ$ over a uv distance from 5.0 k λ to 40.0 k λ . The compactness of the residual phase distribution however is evidence of sufficiently robust phase calibration.

Hull & Plambeck (2015) list the following sources of systematic error in polarization observations with CARMA: i) the need to de-bias linear polarization measurements (Wardle & Kronberg 1974); we apply this correction as noted above; ii) limitations due to polarization leakage uncertainties; iii) absolute EVPA determination accuracy; and, iv) direction-dependent beam polarization (beam squint and beam squash).

Hull & Plambeck (2015) note that EVPA interpretation requires caution for weakly linearly polarized sources ($m_l \leq 0.5\%$). The current data exceed this m_l threshold. However, to verify the accuracy of the absolute EVPA alignment (or equivalently the residual uncorrected R-L phase difference at the reference antenna), we compared the measured EVPA values of the calibrators (3C279, OJ287) in our data against surveys or other contemporaneous observations.

Our current data yielded an error-weighted average EVPA measurement for 3C279 of $36.6^\circ \pm 0.07^\circ$ and $33.9^\circ \pm 0.08^\circ$, and for OJ287 of $-16.5^\circ \pm 0.33^\circ$ and $-19.0^\circ \pm 0.40^\circ$, for the LSB and USB continuum spectral windows respectively. As noted above these 500 MHz spectral windows are centered on ~ 215 GHz and ~ 230 GHz respectively. Applicable external EVPA values were obtained from the MOJAVE project (Lister et al. 2009, private communication), the VLBA-BU-BLAZAR program (Jorstad & Marscher 2016; Jorstad et al. 2017, private communication), and the POLAMI project⁶ (Agudo et al. 2018b,a). We selected external measurements falling within ± 14 days from our observations. Available observations were limited and we considered data within a frequency range of 43.0 \sim 230.5 GHz. The resulting 14-day averaged EVPA for 3C279 thus obtained is $42.88^\circ \pm 10.83^\circ$; and for OJ287 is $159.85^\circ \pm 11.58^\circ$. As a global reference, we note that when averaging over 1000 days the EVPA value obtained for 3C279 is $135.4^\circ \pm 18.3^\circ$ (MOJAVE) and $151.4^\circ \pm 26.0^\circ$ (VLBA-BU-BLAZAR); for OJ287 this global average over 1000 days is $21.5^\circ \pm 4.4^\circ$ (MOJAVE) and $29.3^\circ \pm 17.7^\circ$ (VLBA-BU-BLAZAR). In summary, our measured EVPA of both OJ287 and 3279 were found to be consistent with the external contemporaneous EVPA measurements in broadly comparable frequency bands.

⁴ CARMA project ID: c1217; Observing Block ID: c1217.2D_2303c279.2

⁵ <http://www.scipy.org>

⁶ <http://polami.iaa.es>

For (iv), beam squint is embodied in a double-lobed pattern in Stokes V maps, while beam squash is evident as a cloverleaf pattern in the Stokes Q and U maps (Hull & Plambeck 2015). At $\lambda \sim 1.3\text{mm}$ wavelength, the FWHM of the primary beam for the CARMA 10-m antennas is $\sim 30''$, and for the 6-m antennas it is $\sim 56''$ (Hull & Plambeck 2015). Our source extent is $< 10''$ and on-axis and therefore well within the inner primary beam. Accordingly we do not expect strong primary beam polarization effects. We find no evidence of a quadrupolar squash pattern in the Stokes Q or U images in the current data. We expect our quasar calibrators to have low intrinsic circular polarization (Rybicki & Lightman 1979). The residual Stokes V signal in our calibrators is $m_c \sim 0.32\%$ for 3C279 (in the R Crt observing run), and $m_c \sim 0.77\%$ for OJ287 (in the R Leo observing run) after full calibration. To zeroth-order we assume $\sigma_{m_c} \sim \sigma_{m_l}$ and $\bar{m}_c \sim 0$ and conservatively estimate an approximate intrinsic linear polarization accuracy $\sigma_{m_l} \sim 0.3 - 0.8\%$ accordingly. In practice the calibrators have low, but non-zero circular polarization (Agudo et al. 2018b), amongst other factors and this is an approximate estimate only.

B. CSE PARAMETERS

Detailed modeling of the kinematics, dynamics, and chemical structure in the CSE requires numerical approaches (Bowen 1988; Humphreys et al. 1996; Ireland et al. 2008, 2011) given the inherent complexity of pulsation shock structure, mass loss, and chemistry in this region. However, the G-K modeling in the current work allows use of input profiles from prior semi-analytic models of the CSE, as described further in this Appendix.

The G-K effect allows study of the AGB CSE at different depths due to molecular stratification by chemical abundance and radiative excitation effects. The mean CO distribution extends broadly from the photospheric radius ($\sim 1R_*$) to the outer circumstellar envelope ($\gtrsim 10^4R_*$) (Höfner & Olofsson 2018), with an assumed constant mean fractional abundance $X_{CO} = \left(\frac{n_{CO}}{n_{H_2}}\right)$ (Duari et al. 1999; Decin et al. 2010) until the outer photo-dissociation radius; this encompasses a diverse range of local conditions however. In contrast, SiO is prone to depletion in the inner CSE including due to adsorption onto dust grains (Teyssier et al. 2006; Decin et al. 2010; Gail & Sedlmayr 2013; Gobrecht et al. 2016). In W Hya the SiO e-folding radius is $r_e \sim 85R_*$ (González Delgado et al. 2003; Khouri et al. 2014), with dissipation at radius $r \sim 200R_*$ (Khouri et al. 2014). Modeling of IK Tau by Decin et al. (2010) shows a depletion of SiO by a factor ~ 40 at $r \sim 180R_*$, with an outer photo-dissociation accordingly well within CO.

B.1. Temperature profile

Power-law temperature profile—Following Bowen (1988) as cited by Cherchneff et al. (1992), the kinetic temperature dependence on radius is approximated as a power-law:

$$\frac{T(r)}{T(R_*)} = \left(\frac{r}{R_*}\right)^{-\alpha} \quad (\text{B1})$$

where the exponent index, α , is often adopted to be 0.6 (Cherchneff et al. 1992; Decin et al. 2010; Gobrecht et al. 2016). The functional form of this relation can be derived from the assumption of radiative equilibrium and a gray stellar atmosphere (Bowen 1988). For R Leo the effective stellar blackbody temperature T_* is estimated from modeling of the spectral energy distribution (SED) to be $T_* = 1.8 \times 10^3 K$ (Schöier et al. 2013; Danilovich et al. 2015). We adopt an inner dust condensation radius $R_c \sim 1.6 \times 10^{14}$ cm from SED modeling (Danilovich et al. 2015). These parameters predict a thermal temperature at the dust-condensation radius $T(R_c) \sim 5.3 \times 10^2 K$.

B.2. Density profile

Semi-analytic solutions exist for approximate conditions within broad radial zones in the CSE. We adopt an inner region, extending from the photosphere to the dust formation radius R_c , and an intermediate-outer CSE region extending beyond R_c to the outer edge of the photodissociation zone, and imposing continuity in the density relation.

I. Inner CSE—The inner CSE includes the shock formation radius R_0 (Hill & Willson 1979). We adopt the functional form of the radial density profile $n(r)$ in the shock-extended region derived by Cherchneff et al. (1992, eq.17) by considering averaged physical quantities in the momentum equation. Further, Cherchneff et al. (1992) derive an expression for R_0 using numerical model results from Willson & Bowen (1986). This expression supports the approximation $R_0 \sim R_*$, which we adopt here.

II. Intermediate-outer CSE—In this region we assume the velocity $v_\beta(r)$ is governed by the classical β -law (Lamers & Cassinelli 1999; Danilovich et al. 2015); this yields a velocity gradient:

$$\frac{dv_\beta}{dr} = \frac{\beta}{r} \left[v_c + (v_\infty - v_c) \left(1 - \frac{R_c}{r}\right)^{\beta-1} - v_c - (v_\infty - v_c) \left(1 - \frac{R_c}{r}\right)^\beta \right] \equiv \frac{\beta}{r} [v_{\beta-1} - v_\beta] \quad (\text{B2})$$

where v_c is the expansion velocity at R_c and v_∞ is the terminal expansion velocity. Typically $v_c \sim 3$ km/s based on the approximate sound speed at this radius (Danilovich et al. 2015). We assume $v_\infty \sim \text{const.}$, with $v_\infty \sim 8.5$ km/s for R Leo and $v_\infty \sim 12.0$ km/s for R Crt in CO emission (Danilovich et al. 2015). We adopt a range in velocity exponent index $\beta = 0 \sim 5$ (Danilovich et al. 2015); where $\beta = 0$ implies constant isotropic outflow.

Continuity in the equation of mass yields,

$$\frac{d\rho}{dr} + \frac{\rho}{r} \left[(2 - \beta) + \beta \cdot \frac{v_{\beta-1}}{v_\beta} \right] = 0 \quad (\text{B3})$$

where the quasi-static state and zeroth-order approximation $\vec{v} = v\hat{r}$ is assumed.

We used the SciPy⁷ package `odeint` to solve the differential equation in Equation B3 for $n(r)$ imposing continuity across the inner-region boundary at $r = R_c$. We model the CSE of R Leo in this manner, adopting parameters: $R_* = 1.4$ AU (De Beck et al. 2010), $T_* = 1800$ K, (Schöier et al. 2013), $R_c = 10.7$ AU (Danilovich et al. 2015), $v_\infty = 8.5$ km/s (Danilovich et al. 2015), and $\dot{M} = 1.1 \times 10^{-7} M_\odot/\text{yr}$ (Danilovich et al. 2015). Photospheric temperature estimates in the literature fall in the ranges $T_* \sim 1800 - 2100$ K (Schöier et al. 2013; Ramstedt & Olofsson 2014; González Delgado et al. 2003) and $T_* \sim 2850 - 2890$ K (De Beck et al. 2010; Vlemmings et al. 2019).

The boundary condition continuity was enforced by estimating the number density at the dust condensation radius as $n(R_c) = \frac{\dot{M}}{4\pi R_c^2 v_c}$, assuming a photospheric density 10^{14} cm^{-3} (Gobrecht et al. 2016), and adopting the functional form of the inner CSE density profile (Cherchneff et al. 1992) discussed above.

The derived profiles in velocity, density, and temperature for R Leo are displayed in Fig. 10; they are developed as required input to the G-K modeling only. The derived CSE parameter sets (temperature $T(r)$ and H_2 number density $n(r)$ profiles) are summarized in Table 6. For the G-K modeling we assume that we lie within the CO photo-dissociation radius. In the G-K modeling, the general H_2 density defines the collisional partner for CO but the modeling is not highly sensitive to the exact CO abundance ratio assumed.

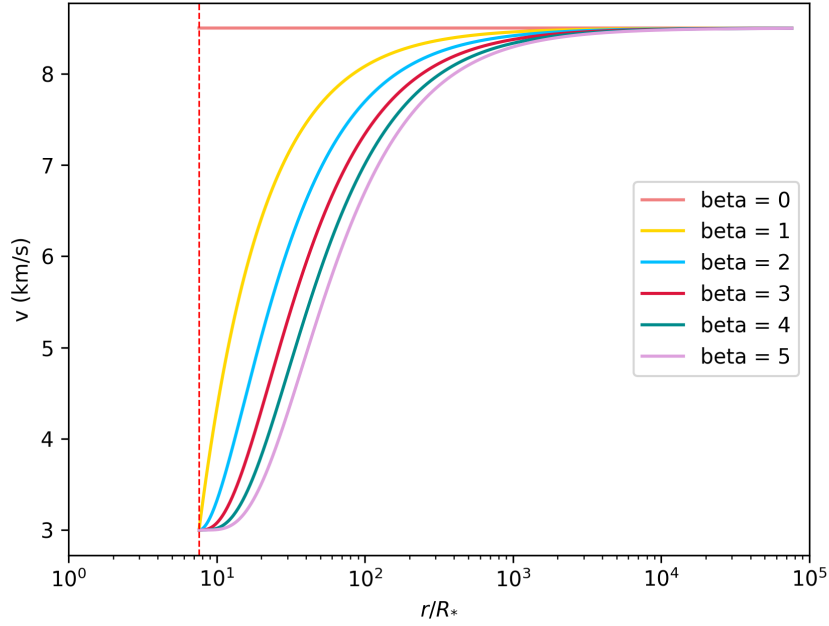
The semi-analytic CSE models do not include spectral line excitation or emission. However, the adopted mass-loss rate and CO outflow kinematics should be consistent with the predicted CO emission intensity. Recent modeling initiatives in the literature to estimate the mass loss rate \dot{M} for R Leo from CO emission parameters are enumerated in Table 7; we refer the reader to these papers for further details of each model. The parameters are as defined above. We have applied our CSE model to each set k of parameters in Table 7 to derive predicted density profiles $n_k(r)$. The maxima and minima of $n_k(r)$ over k are listed in Table 8 at the radii sampled in Table 6; these density ranges are broadly consistent. We therefore believe that the density profiles predicted by our CSE model are conservative but reasonable estimates within the uncertainty in \dot{M} .

Table 6. The radial profiles in temperature $T(r)$, density $n(r)$, and velocity (as represented by parameter β in Equation B2), generated from the CSE analytic models.

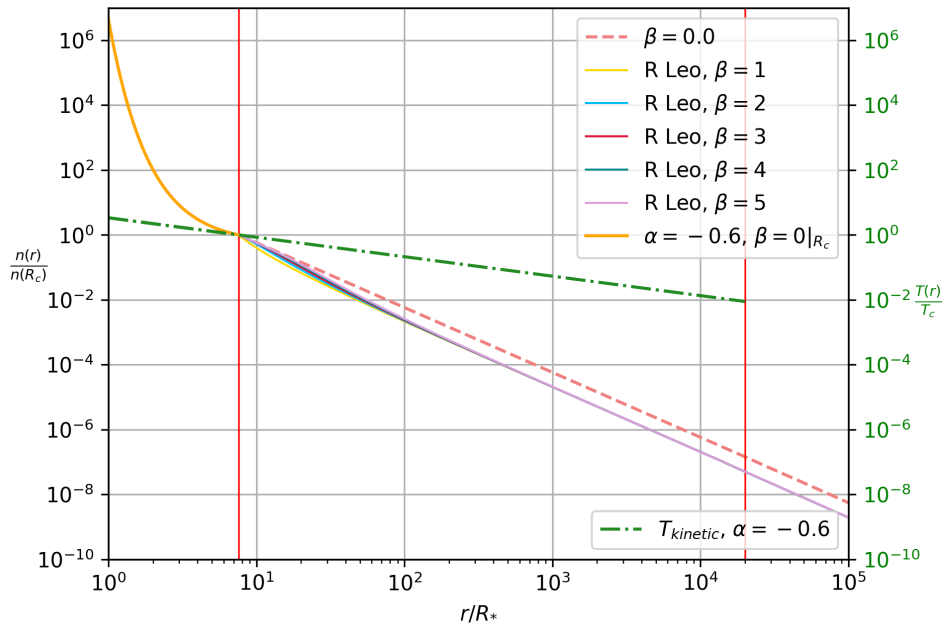
Source	r	T	$n(r)^a$	β
	[R_*]	[K]	[cm^{-3}]	
R Leo	567.1	40	$[1.38 \times 10^3, 3.88 \times 10^3]$	{0, 1, ..., 5}
	392.9	50	$[2.90 \times 10^3, 8.11 \times 10^3]$	{0, 1, ..., 5}
	289.0	60	$[5.39 \times 10^3, 1.50 \times 10^4]$	{0, 1, ..., 5}
	123.2	100	$[2.99 \times 10^4, 8.13 \times 10^4]$	{0, 1, ..., 5}
	19.9	300	$[1.50 \times 10^6, 3.19 \times 10^6]$	{0, 1, ..., 5}

^aThe density $n(r)$ is shown as a minimum and maximum range across the set of integer values of $\beta \in \{0, 1, \dots, 5\}$ enumerated.

⁷ <https://www.scipy.org>



(a) Velocity profile for the range $\beta = 0 \sim 5$ and based on the adopted physical parameters of R Leo.



(b) Density and temperature profile based on the listed physical parameters of R Leo. The left vertical axis labels the normalized number density, $\frac{n(r)}{n(R_c)}$. The vertical axis on the right marks the scale for the normalized temperature profile $\frac{T(r)}{T_c}$. The green dash-dotted line portrays the calculated temperature profile. The red dashed line is the density profile for a model with $\beta = 0$ and $v_\infty = 3.0$ km/s. The remaining density profile lines overlap significantly at larger $\frac{r}{R_*}$ and include models with $\beta \neq 0$, $v_c = 3.0$ km/s, $v_\infty = 8.5$ km/s.

Figure 10. CSE parameters as GK modeling input.

Table 7. CO emission models for R Leo.

v_c	v_∞	β	\dot{M}	Reference
[km/s]	[km/s]		[$10^{-7} M_\odot/\text{yr}$]	
3.0	8.5	5.0	1.1	Danilovich et al. (2015)
-	5.0	0	1.8	Schöier et al. (2013)
-	6.0	0	1.0	Ramstedt & Olofsson (2014)
-	6.0	0	2.0	González Delgado et al. (2003)
-	6.0	0	1.2	Teyssier et al. (2006)
-	9.0	0	0.92	De Beck et al. (2010)

Table 8. Minima and maxima in the radial density profiles $n_k(r)$ across the CO emission models tabulated in Table 7 sampled at or very near the radii listed in Table 6.

Source	r	T	$n_{\min}(r)$	$n_{\max}(r)$
	[R_*]	[K]	[cm^{-3}]	[cm^{-3}]
R Leo	567.1	40	1.75×10^3	3.82×10^3
	392.9	50	3.72×10^3	7.95×10^3
	289.0	60	6.74×10^3	1.47×10^4
	123.2	100	3.71×10^4	8.09×10^4
	19.9	300	1.45×10^6	3.11×10^6

ACKNOWLEDGEMENT

This material is based upon work supported by the National Science Foundation under grant no. NSF-AST 1139950. We thank our colleague, Robert Harris, for his advice and assistance during this project. We thank Roy Lankhaar for collaborative and helpful discussions. This paper makes use of the following ALMA data: ADS/JAO.ALMA#2011.0.00001.CAL. ALMA is a partnership of ESO (representing its member states), NSF (USA) and NINS (Japan), together with NRC (Canada), MOST and ASIAA (Taiwan), and KASI (Republic of Korea), in cooperation with the Republic of Chile. The Joint ALMA Observatory is operated by ESO, AUI/NRAO and NAOJ. The National Radio Astronomy Observatory is a facility of the National Science Foundation operated under cooperative agreement by Associated Universities, Inc. This research made use of Astropy, a community-developed core Python package for Astronomy (Astropy Collaboration et al. 2013). This research has also made use of data from the MOJAVE database that is maintained by the MOJAVE team (Lister et al. 2018). This study makes use of 43 GHz VLBA data from the VLBA-BU Blazar Monitoring Program (VLBA-BU-BLAZAR⁸), funded by NASA through the Fermi Guest Investigator Program. This paper uses astronomical data from the POLAMI program, which uses the IRAM 30 m telescope. This work has made use of data from the European Space Agency (ESA) mission *Gaia* (<https://www.cosmos.esa.int/gaia>), processed by the *Gaia* Data Processing and Analysis Consortium (DPAC, <https://www.cosmos.esa.int/web/gaia/dpac/consortium>). Funding for the DPAC has been provided by national institutions, in particular the institutions participating in the *Gaia* Multilateral Agreement.

Software: CADRE (Friedel 2013), MIRIAD (Sault et al. 1995), SciPy (Virtanen et al. 2019), Astropy (Astropy Collaboration et al. 2013), APLpy (Robitaille & Bressert 2012), Matplotlib (Hunter 2007), NumPy (Oliphant 2006; van der Walt et al. 2011)

⁸ <http://www.bu.edu/blazars/VLBAproject.html>

REFERENCES

- Agudo, I., Thum, C., Ramakrishnan, V., et al. 2018a, *MNRAS*, 473, 1850, doi: [10.1093/mnras/stx2437](https://doi.org/10.1093/mnras/stx2437)
- Agudo, I., Thum, C., Molina, S. N., et al. 2018b, *MNRAS*, 474, 1427, doi: [10.1093/mnras/stx2435](https://doi.org/10.1093/mnras/stx2435)
- Akeson, R. L. 1997, PhD thesis, CALIFORNIA INSTITUTE OF TECHNOLOGY
- Astropy Collaboration, Robitaille, T. P., Tollerud, E. J., et al. 2013, *A&A*, 558, A33, doi: [10.1051/0004-6361/201322068](https://doi.org/10.1051/0004-6361/201322068)
- Balick, B., & Frank, A. 2002, *ARA&A*, 40, 439, doi: [10.1146/annurev.astro.40.060401.093849](https://doi.org/10.1146/annurev.astro.40.060401.093849)
- Blackman, E. G., Frank, A., Markiel, J. A., Thomas, J. H., & Van Horn, H. M. 2001, *Nature*, 409, 485, doi: [10.1038/35054008](https://doi.org/10.1038/35054008)
- Bowen, G. H. 1988, *ApJ*, 329, 299, doi: [10.1086/166378](https://doi.org/10.1086/166378)
- Bower, G. C. 2014, in American Astronomical Society Meeting Abstracts, Vol. 223, American Astronomical Society Meeting Abstracts #223, 108.02
- Cherchneff, I., Barker, J. R., & Tielens, A. G. G. M. 1992, *ApJ*, 401, 269, doi: [10.1086/172059](https://doi.org/10.1086/172059)
- Ching, T.-C., Lai, S.-P., Zhang, Q., et al. 2016, *ApJ*, 819, 159, doi: [10.3847/0004-637X/819/2/159](https://doi.org/10.3847/0004-637X/819/2/159)
- Cortes, P. C., Crutcher, R. M., & Watson, W. D. 2005, *ApJ*, 628, 780, doi: [10.1086/430815](https://doi.org/10.1086/430815)
- Cotton, W. D., Ragland, S., Pluzhnik, E., et al. 2009, *ApJ*, 704, 170, doi: [10.1088/0004-637X/704/1/170](https://doi.org/10.1088/0004-637X/704/1/170)
- Cox, N. L. J., Kerschbaum, F., van Marle, A.-J., et al. 2012, *A&A*, 537, A35, doi: [10.1051/0004-6361/201117910](https://doi.org/10.1051/0004-6361/201117910)
- Crutcher, R. M. 2012, *ARA&A*, 50, 29, doi: [10.1146/annurev-astro-081811-125514](https://doi.org/10.1146/annurev-astro-081811-125514)
- Crutcher, R. M., & Kemball, A. J. 2019, *Frontiers in Astronomy and Space Sciences*, 6, 66, doi: [10.3389/fspas.2019.00066](https://doi.org/10.3389/fspas.2019.00066)
- Danilovich, T., Teyssier, D., Justtanont, K., et al. 2015, *A&A*, 581, A60, doi: [10.1051/0004-6361/201526705](https://doi.org/10.1051/0004-6361/201526705)
- De Beck, E., Decin, L., de Koter, A., et al. 2010, *A&A*, 523, A18, doi: [10.1051/0004-6361/200913771](https://doi.org/10.1051/0004-6361/200913771)
- de Vicente, P., Bujarrabal, V., Díaz-Pulido, A., et al. 2016, *A&A*, 589, A74, doi: [10.1051/0004-6361/201527174](https://doi.org/10.1051/0004-6361/201527174)
- Decin, L., De Beck, E., Brünken, S., et al. 2010, *A&A*, 516, A69, doi: [10.1051/0004-6361/201014136](https://doi.org/10.1051/0004-6361/201014136)
- Deguchi, S., & Watson, W. D. 1984, *ApJ*, 285, 126, doi: [10.1086/162483](https://doi.org/10.1086/162483)
- Diamond, P. J., & Kemball, A. J. 2003, *ApJ*, 599, 1372, doi: [10.1086/379347](https://doi.org/10.1086/379347)
- Diamond, P. J., Kemball, A. J., Junor, W., et al. 1994, *ApJL*, 430, L61, doi: [10.1086/187438](https://doi.org/10.1086/187438)
- Dorch, S. B. F. 2004, *A&A*, 423, 1101, doi: [10.1051/0004-6361:20040435](https://doi.org/10.1051/0004-6361:20040435)
- Duari, D., Cherchneff, I., & Willacy, K. 1999, *A&A*, 341, L47. <https://arxiv.org/abs/astro-ph/9811263>
- Duthu, A., Herpin, F., Wiesemeyer, H., et al. 2017, *A&A*, 604, A12, doi: [10.1051/0004-6361/201730485](https://doi.org/10.1051/0004-6361/201730485)
- Elitzur, M. 1980, *ApJ*, 240, 553, doi: [10.1086/158260](https://doi.org/10.1086/158260)
- . 1996, *ApJ*, 457, 415, doi: [10.1086/176741](https://doi.org/10.1086/176741)
- Etoka, S., & Le Squeren, A. M. 1997, *A&A*, 321, 877
- Feast, M. W., Glass, I. S., Whitelock, P. A., & Catchpole, R. M. 1989, *MNRAS*, 241, 375, doi: [10.1093/mnras/241.3.375](https://doi.org/10.1093/mnras/241.3.375)
- Fiebig, D., & Guesten, R. 1989, *A&A*, 214, 333
- Fish, V. L., Reid, M. J., Menten, K. M., & Pillai, T. 2006, *A&A*, 458, 485, doi: [10.1051/0004-6361:20065379](https://doi.org/10.1051/0004-6361:20065379)
- Flower, D. R. 2001, *Journal of Physics B Atomic Molecular Physics*, 34, 2731, doi: [10.1088/0953-4075/34/13/315](https://doi.org/10.1088/0953-4075/34/13/315)
- Frank, A., Balick, B., Icke, V., & Mellema, G. 1993, *ApJL*, 404, L25, doi: [10.1086/186735](https://doi.org/10.1086/186735)
- Frank, A., Chen, Z., Reichardt, T., et al. 2018, *Galaxies*, 6, 113, doi: [10.3390/galaxies6040113](https://doi.org/10.3390/galaxies6040113)
- Friedel, D. N. 2013, *Astronomy and Computing*, 2, 74, doi: [10.1016/j.ascom.2013.09.003](https://doi.org/10.1016/j.ascom.2013.09.003)
- Gaia Collaboration, Brown, A. G. A., Vallenari, A., et al. 2018, *A&A*, 616, A1, doi: [10.1051/0004-6361/201833051](https://doi.org/10.1051/0004-6361/201833051)
- Gail, H.-P., & Sedlmayr, E. 2013, *Physics and Chemistry of Circumstellar Dust Shells* (Cambridge University Press)
- García-Segura, G., Langer, N., Różyńska, M., & Franco, J. 1999, *ApJ*, 517, 767, doi: [10.1086/307205](https://doi.org/10.1086/307205)
- García-Segura, G., Ricker, P. M., & Taam, R. E. 2018, *ApJ*, 860, 19, doi: [10.3847/1538-4357/aac08c](https://doi.org/10.3847/1538-4357/aac08c)
- García-Segura, G., Villaver, E., Langer, N., Yoon, S.-C., & Manchado, A. 2014, *ApJ*, 783, 74, doi: [10.1088/0004-637X/783/2/74](https://doi.org/10.1088/0004-637X/783/2/74)
- Girart, J. M., Patel, N., Vlemmings, W. H. T., & Rao, R. 2012, *ApJL*, 751, L20, doi: [10.1088/2041-8205/751/1/L20](https://doi.org/10.1088/2041-8205/751/1/L20)
- Glenn, J., Jewell, P. R., Fourre, R., & Miaja, L. 2003, *ApJ*, 588, 478, doi: [10.1086/373948](https://doi.org/10.1086/373948)
- Glenn, J., Walker, C. K., Bieging, J. H., & Jewell, P. R. 1997, *ApJ*, 487, L89, doi: [10.1086/310863](https://doi.org/10.1086/310863)
- Gobrecht, D., Cherchneff, I., Sarangi, A., Plane, J. M. C., & Bromley, S. T. 2016, *A&A*, 585, A6, doi: [10.1051/0004-6361/201425363](https://doi.org/10.1051/0004-6361/201425363)
- Goldreich, P., Keeley, D. A., & Kwan, J. Y. 1973, *ApJ*, 179, 111, doi: [10.1086/151852](https://doi.org/10.1086/151852)
- Goldreich, P., & Kylafis, N. D. 1981, *ApJL*, 243, L75, doi: [10.1086/183446](https://doi.org/10.1086/183446)
- . 1982, *ApJ*, 253, 606, doi: [10.1086/159663](https://doi.org/10.1086/159663)
- González Delgado, D., Olofsson, H., Kerschbaum, F., et al. 2003, *A&A*, 411, 123, doi: [10.1051/0004-6361:20031068](https://doi.org/10.1051/0004-6361:20031068)
- Gray, M. 2012, *Maser Sources in Astrophysics*

- Green, S., & Chapman, S. 1978, *ApJS*, 37, 169, doi: [10.1086/190523](https://doi.org/10.1086/190523)
- Hamaker, J. P., Bregman, J. D., & Sault, R. J. 1996, *A&AS*, 117, 137
- Haniff, C. A., Scholz, M., & Tuthill, P. G. 1995, *MNRAS*, 276, 640, doi: [10.1093/mnras/276.2.640](https://doi.org/10.1093/mnras/276.2.640)
- Hartquist, T. W., & Dyson, J. E. 1997, *A&A*, 319, 589
- Herpin, F., Baudry, A., Thum, C., Morris, D., & Wiesemeyer, H. 2006, *A&A*, 450, 667, doi: [10.1051/0004-6361:20054255](https://doi.org/10.1051/0004-6361:20054255)
- Hill, S. J., & Willson, L. A. 1979, *ApJ*, 229, 1029, doi: [10.1086/157038](https://doi.org/10.1086/157038)
- Hoang, T., & Lazarian, A. 2008, *MNRAS*, 388, 117, doi: [10.1111/j.1365-2966.2008.13249.x](https://doi.org/10.1111/j.1365-2966.2008.13249.x)
- Höfner, S., & Olofsson, H. 2018, *A&A Rv*, 26, 1, doi: [10.1007/s00159-017-0106-5](https://doi.org/10.1007/s00159-017-0106-5)
- Hull, C. L. H. 2014, PhD thesis, University of California, Berkeley
- Hull, C. L. H., & Plambeck, R. L. 2015, *Journal of Astronomical Instrumentation*, 4, 1550005, doi: [10.1142/S2251171715500051](https://doi.org/10.1142/S2251171715500051)
- Humphreys, E. M. L., Gray, M. D., Yates, J. A., et al. 1996, *MNRAS*, 282, 1359, doi: [10.1093/mnras/282.4.1359](https://doi.org/10.1093/mnras/282.4.1359)
- Hunter, J. D. 2007, *Computing in Science & Engineering*, 9, 90, doi: [10.1109/MCSE.2007.55](https://doi.org/10.1109/MCSE.2007.55)
- Ireland, M. J., Scholz, M., & Wood, P. R. 2008, *MNRAS*, 391, 1994, doi: [10.1111/j.1365-2966.2008.14037.x](https://doi.org/10.1111/j.1365-2966.2008.14037.x)
- . 2011, *MNRAS*, 418, 114, doi: [10.1111/j.1365-2966.2011.19469.x](https://doi.org/10.1111/j.1365-2966.2011.19469.x)
- Ireland, M. J., Tuthill, P. G., Bedding, T. R., Robertson, J. G., & Jacob, A. P. 2004, *MNRAS*, 350, 365, doi: [10.1111/j.1365-2966.2004.07651.x](https://doi.org/10.1111/j.1365-2966.2004.07651.x)
- Ishitsuka, J. K., Imai, H., Omodaka, T., et al. 2001, *PASJ*, 53, 1231, doi: [10.1093/pasj/53.6.1231](https://doi.org/10.1093/pasj/53.6.1231)
- Jorstad, S., & Marscher, A. 2016, *Galaxies*, 4, 47, doi: [10.3390/galaxies4040047](https://doi.org/10.3390/galaxies4040047)
- Jorstad, S. G., Marscher, A. P., Morozova, D. A., et al. 2017, *ApJ*, 846, 98, doi: [10.3847/1538-4357/aa8407](https://doi.org/10.3847/1538-4357/aa8407)
- Kemball, A. J., & Diamond, P. J. 1993, in *Lecture Notes in Physics*, Berlin Springer Verlag, Vol. 412, *Astrophysical Masers*, ed. A. W. Clegg & G. E. Nedoluha, 369–372
- Kemball, A. J., & Diamond, P. J. 1997, *ApJL*, 481, L111, doi: [10.1086/310664](https://doi.org/10.1086/310664)
- Kemball, A. J., Diamond, P. J., Gonidakis, I., et al. 2009, *ApJ*, 698, 1721, doi: [10.1088/0004-637X/698/2/1721](https://doi.org/10.1088/0004-637X/698/2/1721)
- Kemball, A. J., & Richter, L. 2011, *A&A*, 533, A26, doi: [10.1051/0004-6361/201117337](https://doi.org/10.1051/0004-6361/201117337)
- Khouri, T., de Koter, A., Decin, L., et al. 2014, *A&A*, 570, A67, doi: [10.1051/0004-6361/201424298](https://doi.org/10.1051/0004-6361/201424298)
- Khouri, T., Vlemmings, W. H. T., Paladini, C., et al. 2020, *A&A*, 635, A200, doi: [10.1051/0004-6361/201834618](https://doi.org/10.1051/0004-6361/201834618)
- Kim, D.-J., Cho, S.-H., Yun, Y., et al. 2018, *ApJL*, 866, L19, doi: [10.3847/2041-8213/aae58b](https://doi.org/10.3847/2041-8213/aae58b)
- Knight, W. R. 1966, *Journal of the American Statistical Association*, 61, 436
- Kwok, S., Purton, C. R., & Fitzgerald, P. M. 1978, *ApJL*, 219, L125, doi: [10.1086/182621](https://doi.org/10.1086/182621)
- Kylafis, N. D. 1983a, *ApJ*, 267, 137, doi: [10.1086/160851](https://doi.org/10.1086/160851)
- . 1983b, *ApJ*, 275, 135, doi: [10.1086/161520](https://doi.org/10.1086/161520)
- Lai, S.-P., Girart, J. M., & Crutcher, R. M. 2003, *ApJ*, 598, 392, doi: [10.1086/378769](https://doi.org/10.1086/378769)
- Lamers, H. J. G. L. M., & Cassinelli, J. P. 1999, *Introduction to Stellar Winds*, 452
- Lankhaar, B., & Vlemmings, W. 2019, *A&A*, 628, A14, doi: [10.1051/0004-6361/201935064](https://doi.org/10.1051/0004-6361/201935064)
- . 2020, *A&A*, 636, A14, doi: [10.1051/0004-6361/202037509](https://doi.org/10.1051/0004-6361/202037509)
- Lazarian, A. 2007, *JQSRT*, 106, 225, doi: [10.1016/j.jqsrt.2007.01.038](https://doi.org/10.1016/j.jqsrt.2007.01.038)
- Leal-Ferreira, M. L., Vlemmings, W. H. T., Kemball, A., & Amiri, N. 2013, *A&A*, 554, A134, doi: [10.1051/0004-6361/201321218](https://doi.org/10.1051/0004-6361/201321218)
- Lèbre, A., Aurière, M., Fabas, N., et al. 2014, *A&A*, 561, A85, doi: [10.1051/0004-6361/201322826](https://doi.org/10.1051/0004-6361/201322826)
- Lee, C.-F., Hwang, H.-C., Ching, T.-C., et al. 2018, *Nature Communications*, 9, 4636, doi: [10.1038/s41467-018-07143-8](https://doi.org/10.1038/s41467-018-07143-8)
- Li, H.-B., & Henning, T. 2011, *Nature*, 479, 499, doi: [10.1038/nature10551](https://doi.org/10.1038/nature10551)
- Lis, D. C., Goldsmith, P. F., Dickman, R. L., et al. 1988, *ApJ*, 328, 304, doi: [10.1086/166293](https://doi.org/10.1086/166293)
- Lister, M. L., Aller, M. F., Aller, H. D., et al. 2018, *ApJS*, 234, 12, doi: [10.3847/1538-4365/aa9c44](https://doi.org/10.3847/1538-4365/aa9c44)
- Lister, M. L., Aller, H. D., Aller, M. F., et al. 2009, *AJ*, 137, 3718, doi: [10.1088/0004-6256/137/3/3718](https://doi.org/10.1088/0004-6256/137/3/3718)
- Lovas, F. J., Bass, J. E., Dragoset, R. A., & Olsen, K. J. 2009, doi: [10.18434/T4JP4Q](https://doi.org/10.18434/T4JP4Q)
- Luri, X., Brown, A. G. A., Sarro, L. M., et al. 2018, *A&A*, 616, A9, doi: [10.1051/0004-6361/201832964](https://doi.org/10.1051/0004-6361/201832964)
- Matt, S., Balick, B., Winglee, R., & Goodson, A. 2000, *ApJ*, 545, 965, doi: [10.1086/317843](https://doi.org/10.1086/317843)
- Matthews, L. D., Reid, M. J., Menten, K. M., & Akiyama, K. 2018, *AJ*, 156, 15, doi: [10.3847/1538-3881/aac491](https://doi.org/10.3847/1538-3881/aac491)
- Menten, K. M., & Melnick, G. J. 1991, *ApJ*, 377, 647, doi: [10.1086/170392](https://doi.org/10.1086/170392)
- Miyoshi, M., Matsumoto, K., Kameno, S., Takaba, H., & Lwata, T. 1994, *Nature*, 371, 395, doi: [10.1038/371395a0](https://doi.org/10.1038/371395a0)
- Moran, J. M., Ball, J. A., Hansen, S. S., et al. 1979, *ApJL*, 231, L67, doi: [10.1086/183006](https://doi.org/10.1086/183006)

- Morris, M., Lucas, R., & Omont, A. 1985, *A&A*, 142, 107
- Nordhaus, J., & Blackman, E. G. 2006, *MNRAS*, 370, 2004, doi: [10.1111/j.1365-2966.2006.10625.x](https://doi.org/10.1111/j.1365-2966.2006.10625.x)
- Nordhaus, J., Blackman, E. G., & Frank, A. 2007, *MNRAS*, 376, 599, doi: [10.1111/j.1365-2966.2007.11417.x](https://doi.org/10.1111/j.1365-2966.2007.11417.x)
- Oliphant, T. E. 2006, *A guide to NumPy*, Vol. 1 (Trelgol Publishing USA)
- Paladini, C., Klotz, D., Sacuto, S., et al. 2017, *A&A*, 600, A136, doi: [10.1051/0004-6361/201527210](https://doi.org/10.1051/0004-6361/201527210)
- Pardo, J. R., Alcolea, J., Bujarrabal, V., et al. 2004, *A&A*, 424, 145, doi: [10.1051/0004-6361:20040309](https://doi.org/10.1051/0004-6361:20040309)
- Pearson, K. 1895, *Proceedings of the Royal Society of London Series I*, 58, 240
- Petit, P., Aurière, M., Konstantinova-Antova, R., et al. 2013, *Magnetic Fields and Convection in the Cool Supergiant Betelgeuse*, ed. J.-P. Rozelot & C. E. . Neiner, 231
- Proust, D., Ochsenbein, F., & Pettersen, B. R. 1981, *A&AS*, 44, 179
- Ramstedt, S., & Olofsson, H. 2014, *A&A*, 566, A145, doi: [10.1051/0004-6361/201423721](https://doi.org/10.1051/0004-6361/201423721)
- Ramstedt, S., Doan, L., Danilovich, T., et al. 2020, doi: [10.1051/0004-6361/201936874](https://doi.org/10.1051/0004-6361/201936874)
- Reid, M. J. 1990, in *IAU Symposium*, Vol. 140, *Galactic and Intergalactic Magnetic Fields*, ed. R. Beck, P. P. Kronberg, & R. Wielebinski, 21–24
- Reid, M. J. 2007, in *IAU Symposium*, Vol. 242, *Astrophysical Masers and their Environments*, ed. J. M. Chapman & W. A. Baan, 522–529
- Reid, M. J., & Menten, K. M. 2007, *ApJ*, 671, 2068, doi: [10.1086/523085](https://doi.org/10.1086/523085)
- Reid, M. J., & Moran, J. M. 1981, *ARA&A*, 19, 231, doi: [10.1146/annurev.aa.19.090181.001311](https://doi.org/10.1146/annurev.aa.19.090181.001311)
- Reid, M. J., Moran, J. M., Leach, R. W., et al. 1979, *ApJL*, 227, L89, doi: [10.1086/182873](https://doi.org/10.1086/182873)
- Richter, L., Kembell, A., & Jonas, J. 2016, *MNRAS*, 461, 2309, doi: [10.1093/mnras/stw1302](https://doi.org/10.1093/mnras/stw1302)
- Robinson, S. E., & van Blerkom, D. J. 1981, *ApJ*, 249, 566, doi: [10.1086/159316](https://doi.org/10.1086/159316)
- Robitaille, T., & Bressert, E. 2012, *APLpy: Astronomical Plotting Library in Python*. <http://ascl.net/1208.017>
- Rüdiger, G., Hollerbach, R., & Kulsrud, R. M. 2005, *Physics Today*, 58, 56, doi: [10.1063/1.2155763](https://doi.org/10.1063/1.2155763)
- Rybicki, G. B., & Lightman, A. P. 1979, *Radiative processes in astrophysics*
- Sabin, L., Zhang, Q., Zijlstra, A. A., et al. 2014, *MNRAS*, 438, 1794, doi: [10.1093/mnras/stt2318](https://doi.org/10.1093/mnras/stt2318)
- Samus', N. N., Kazarovets, E. V., Durlevich, O. V., Kireeva, N. N., & Pastukhova, E. N. 2017, *Astronomy Reports*, 61, 80, doi: [10.1134/S1063772917010085](https://doi.org/10.1134/S1063772917010085)
- Sault, R. J., Hamaker, J. P., & Bregman, J. D. 1996, *A&AS*, 117, 149
- Sault, R. J., Teuben, P. J., & Wright, M. C. H. 1995, in *Astronomical Society of the Pacific Conference Series*, Vol. 77, *Astronomical Data Analysis Software and Systems IV*, ed. R. A. Shaw, H. E. Payne, & J. J. E. Hayes, 433
- Schöier, F. L., Ramstedt, S., Olofsson, H., et al. 2013, *A&A*, 550, A78, doi: [10.1051/0004-6361/201220400](https://doi.org/10.1051/0004-6361/201220400)
- Schöier, F. L., van der Tak, F. F. S., van Dishoeck, E. F., & Black, J. H. 2005, *A&A*, 432, 369, doi: [10.1051/0004-6361:20041729](https://doi.org/10.1051/0004-6361:20041729)
- Shinnaga, H., Moran, J. M., Young, K. H., & Ho, P. T. P. 2004, *ApJL*, 616, L47, doi: [10.1086/425133](https://doi.org/10.1086/425133)
- Sobolev, V. V. 1960, *Moving envelopes of stars*
- Soker, N. 2002, *MNRAS*, 336, 826, doi: [10.1046/j.1365-8711.2002.05817.x](https://doi.org/10.1046/j.1365-8711.2002.05817.x)
- Soker, N. 2004, in *Astronomical Society of the Pacific Conference Series*, Vol. 313, *Asymmetrical Planetary Nebulae III: Winds, Structure and the Thunderbird*, ed. M. Meixner, J. H. Kastner, B. Balick, & N. Soker, 562
- Soker, N. 2006, *Publications of the Astronomical Society of the Pacific*, 118, 260
- Soker, N., & Zoabi, E. 2002, *MNRAS*, 329, 204, doi: [10.1046/j.1365-8711.2002.05021.x](https://doi.org/10.1046/j.1365-8711.2002.05021.x)
- Szymczak, M., Cohen, R. J., & Richards, A. M. S. 1999, *MNRAS*, 304, 877, doi: [10.1046/j.1365-8711.1999.02365.x](https://doi.org/10.1046/j.1365-8711.1999.02365.x)
- Taylor, J. R. 1996, *An Introduction to Error Analysis: The Study of Uncertainties in Physical Measurements 2nd Edition* (University Science Books), 327
- Teyssier, D., Hernandez, R., Bujarrabal, V., Yoshida, H., & Phillips, T. G. 2006, *A&A*, 450, 167, doi: [10.1051/0004-6361:20053759](https://doi.org/10.1051/0004-6361:20053759)
- Thomas, J. H., Markiel, J. A., & van Horn, H. M. 1995, *ApJ*, 453, 403, doi: [10.1086/176400](https://doi.org/10.1086/176400)
- Thompson, A. R., Moran, J. M., & Swenson, George W., J. 2017, *Interferometry and Synthesis in Radio Astronomy*, 3rd Edition, doi: [10.1007/978-3-319-44431-4](https://doi.org/10.1007/978-3-319-44431-4)
- van der Walt, S., Colbert, S. C., & Varoquaux, G. 2011, *Computing in Science and Engineering*, 13, 22, doi: [10.1109/MCSE.2011.37](https://doi.org/10.1109/MCSE.2011.37)
- van Langevelde, H., Quiroga-Nuñez, L. H., Vlemmings, W. H. T., et al. 2018, in *14th European VLBI Network Symposium & Users Meeting (EVN 2018)*, 43
- van Marle, A. J., Cox, N. L. J., & Decin, L. 2014, *A&A*, 570, A131, doi: [10.1051/0004-6361/201424452](https://doi.org/10.1051/0004-6361/201424452)
- Virtanen, P., Gommers, R., Oliphant, T. E., et al. 2019, *arXiv e-prints*, arXiv:1907.10121. <https://arxiv.org/abs/1907.10121>

- Vlemmings, W. 2019, in IAU Symposium, Vol. 343, IAU Symposium, ed. F. Kerschbaum, M. Groenewegen, & H. Olofsson, 19–26
- Vlemmings, W. H. T., Diamond, P. J., & Imai, H. 2006, *Nature*, 440, 58, doi: [10.1038/nature04466](https://doi.org/10.1038/nature04466)
- Vlemmings, W. H. T., Humphreys, E. M. L., & Franco-Hernández, R. 2011, *ApJ*, 728, 149, doi: [10.1088/0004-637X/728/2/149](https://doi.org/10.1088/0004-637X/728/2/149)
- Vlemmings, W. H. T., Khouri, T., & Olofsson, H. 2019, *A&A*, 626, A81, doi: [10.1051/0004-6361/201935329](https://doi.org/10.1051/0004-6361/201935329)
- Vlemmings, W. H. T., Ramstedt, S., Rao, R., & Maercker, M. 2012, *A&A*, 540, L3, doi: [10.1051/0004-6361/201218897](https://doi.org/10.1051/0004-6361/201218897)
- Vlemmings, W. H. T., Khouri, T., Martí-Vidal, I., et al. 2017, *A&A*, 603, A92, doi: [10.1051/0004-6361/201730735](https://doi.org/10.1051/0004-6361/201730735)
- Wannier, P. G., Scoville, N. Z., & Barvainis, R. 1983, *ApJ*, 267, 126, doi: [10.1086/160850](https://doi.org/10.1086/160850)
- Wardle, J. F. C., & Kronberg, P. P. 1974, *ApJ*, 194, 249, doi: [10.1086/153240](https://doi.org/10.1086/153240)
- Watson, W. D. 2009, in *Revista Mexicana de Astronomía y Astrofísica Conference Series*, Vol. 36, *Revista Mexicana de Astronomía y Astrofísica Conference Series*, 113–120
- Whitelock, P., & Feast, M. 2000, *MNRAS*, 319, 759, doi: [10.1046/j.1365-8711.2000.03742.x](https://doi.org/10.1046/j.1365-8711.2000.03742.x)
- Wiesemeyer, H., Thum, C., Baudry, A., & Herpin, F. 2009, *A&A*, 498, 801, doi: [10.1051/0004-6361/200811242](https://doi.org/10.1051/0004-6361/200811242)
- Willson, L. A., & Bowen, G. H. 1986, *Stellar Pulsation, Atmospheric Structure, and Mass Loss*, ed. M. Zeilik & D. M. Gibson, Vol. 254, 385
- Wittkowski, M., Chiavassa, A., Freytag, B., et al. 2016, *A&A*, 587, A12, doi: [10.1051/0004-6361/201527614](https://doi.org/10.1051/0004-6361/201527614)
- Xu, S., Zhang, B., Reid, M. J., Zheng, X., & Wang, G. 2019, *ApJ*, 875, 114, doi: [10.3847/1538-4357/ab0e83](https://doi.org/10.3847/1538-4357/ab0e83)
- Yang, L., & Lai, S. P. 2010, in *JTAM*, Vol. 8, *ASRROC 2010 Symposium Proceedings: Probing the magnetic field structure in star-forming regions through molecular line polarization*
- Yates, J. A., Cohen, R. J., & Hills, R. E. 1995, *MNRAS*, 273, 529, doi: [10.1093/mnras/273.3.529](https://doi.org/10.1093/mnras/273.3.529)
- Zwillinger, D., & Kokoska, S. 1999, *CRC standard probability and statistics tables and formulae*, 568